A comparison of different approaches to estimate the efficiency of Wells turbines

F. Licheri*, T. Ghisu, F. Cambuli, P. Puddu
Department of Mechanical, Chemical and Materials Engineering
University of Cagliari
Cagliari, Via Marengo 2, 09123, Italy

ABSTRACT

Wells turbines are among the most interesting power take-off devices used in Oscillating Water Column (OWC) systems for the conversion of sea wave energy into electrical energy. Several configurations have been studied during the last decades, both experimentally and numerically. Different methodologies have been proposed to estimate the efficiency of this turbine, as well as different approaches to evaluate the intermediate quantities required.

Recent works have evaluated the so-called second-law efficiency of a Wells turbine, and compared it to the more often used first-law efficiency. In this study, theoretical analyses and numerical simulations have been used to demonstrate how these two efficiency measures should lead to equivalent values, given the low pressure ratio of the machine. In numerical simulations, small discrepancies can exist, but they are due to the difficulty of ensuring entropy conservation on complex 3D meshes. The efficiencies of different rotor geometries are analyzed based on the proposed measures, and the main sources of loss are identified.

*Address all correspondence to this author: fabio.licheri@unica.it

NOMENCLATURE

Acronyms

CFL	Courant - Friedrichs - Lewy number
CFD	computational fluid dynamics
CV	control volume
DNS	direct numerical simulation
LE	leading edge
NS	Navier-Stokes
OWC	oscillating water column
PS	pressure side
RANS	Reynolds averaged Navier-Stokes
REAL	realizable
S-A	Spalart Allmaras
SS	suction side
SST	shear-stress transport
STD	standard
TE	trailing edge

Dimensional properties

c	blade chord [m]
E	energy [kg m^2 s^{-2}]
ε	rate of dissipation of k [m^2 s^{-3}]
$\dot{E}_x$	exergy per unit time [kg m^2 s^{-3}]
f	frequency [s^{-1}]
h	enthalpy [kg m^2 s^{-2}]
k	turbulent kinetic energy [m^2 s^{-2}]
λ	thermal conductivity [kg m s^{-3} K^{-1}]
λ	volume viscosity [kg m^{-1} s^{-1}]
μ	dynamic viscosity [kg m^{-1} s^{-1}]
∇^S	sum of gradient and gradient transposed [m^{-1}]
ν	kinematic viscosity [m^2 s^{-1}]
ω	specific dissipation rate [s^{-1}]
Ω	angular rotational frequency [s^{-1}]
Π	stress tensor [kg m^{-1} s^{-2}]
p	pressure [kg m^{-1} s^{-2}]
Q	volumetric flow rate [m^3 s^{-1}]
r	turbine radius [m]
ρ	air density [kg m^{-3}]
s	specific entropy [m^2 s^{-2} K^{-1}]
$\dot{S}_G$	entropy generation rate [kg m^2 s^{-3} K^{-1}]
σ	entropy generation rate per unit mass [m^2 s^{-3} K^{-1}]
T	temperature [K]
t	time [s]
T_w	wave cycle period [s]
$\mathcal{T}$	torque [kg m^2 s^{-2}]
U	blade speed [m s^{-1}]
V	velocity [m s^{-1}]
$\mathcal{V}$	volume [m^3]
$\dot{W}$	work [kg m^2 s^{-3}]
X	turbine tangential force [kg m s^{-2}]
Z	turbine axial force [kg m s^{-2}]

Non-dimensional properties

η	efficiency
f_{v1}	viscous damping function

I	identity tensor	in	input
$K_{\dot{S}}$	entropy generation/dissipation rate	ind	indirect
Re	Reynolds number	is	isentropic
$\mathcal{T}^*$	torque coefficient	$lost$	lost
ϕ	flow coefficient	m	mid radius
p_t^*	total pressure drop coefficient	mf	mean flow
p^*	static pressure drop coefficient	out	output
z	number of blades	pol	polytropic
Subscripts and superscripts		R	Reynolds'
$'$	fluctuating component	ref	reference
$\overline{()}$	mean value	T	turbulent
a	axial	t	total quantity
ad	aerodynamic	tip	blade tip
d	dissipation	ts	*total-to-static*
g	production	tt	*total-to-total*
hub	turbine hub	V	due to fluid flow
II	second-law approach		

1 INTRODUCTION

The growing demand for renewable energy has drawn the attention to the strong potential of sea-wave energy [1]. Among the different technologies that have been studied and tested for the conversion of sea-wave energy into electrical energy, Oscillating Water Column (OWC) systems represent a reliable and simple solution [2]. Fig. 1 (a) presents a schematic of an OWC system, composed of two main units: an open chamber, partially submerged under the sea free surface, where the water movement induces an alternative movement of a column of air, and a turbine driven by the air flow. The periodic inversion of the air flow in the OWC chamber requires a system that is capable of maintaining the same direction of rotation regardless of the direction of the air flow. The Wells turbine, patented by Dr. A. A. Wells in 1970s [3], is characterized by a symmetrical

blade profile staggered at 90 degrees with respect to the axis of rotation, and it represents a solution of self-rectifying air turbine (Fig. 1 (b)) which ensures similar performance during outflow (air flowing out of the chamber) and inflow (air flowing into the chamber).

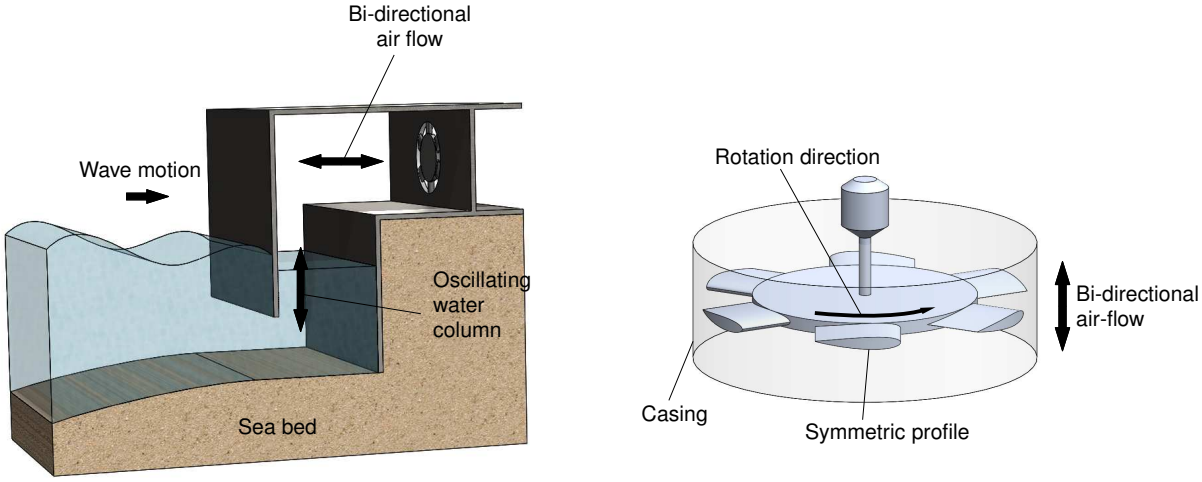

(a) OWC system (b) Wells turbine

Fig. 1. Working principle of a OWC system and a Wells turbine

Owing to their simplicity of construction and reliability, Wells turbines have been widely studied as power-take-offs in OWC systems, both experimentally [4–6] and numerically [7–9]. In recent years, a number of authors [10–13] have analyzed the turbine performance from a second-law point of view, trying to estimate the turbine efficiency based on an exergy balance, evaluating the entropy produced by the air flow through the machine.

One of the limitations of Wells turbines comes from its symmetrical profile, which leads to a limited lift at low incidence angles and the occurrence of stall at high flow coefficients [14], which reduces the operating range of the machine. A number of papers focused on the improvement of the Wells turbine performance not only by extending its operating range [15–17], but also by increasing the efficiency and output torque. Most of the proposed performance improvements are based on a first-law approach [18–20]; more recently some authors investigated new design solutions by looking at the entropy production inside the machine. Shehata *et al.* [10] investigated the entropy generation of several 2D blade profiles frequently used in Wells turbines in unsteady

flow conditions. Nazeryan and Lakzian [12, 21] compared the entropy generated by a rotor with constant and one with variable thickness blades, showing a reduction in entropy production and therefore increased performance in the latter. Shehata *et al.* [22] showed the effect of passive flow control on the onset of stall for a symmetrical 2D profile and the implications on the second-law efficiency.

In this paper, the common definition for the efficiency of a Wells turbine [8, 23–25] is compared with a different evaluation that has been recently introduced and is based on a second law analysis [10–12, 21, 22]. A theoretical derivation and numerical results from CFD simulations are used to demonstrate how the two definitions lead to equivalent results, under the assumptions used for this type of turbomachines. Different models for turbulence closure have been compared, not only with respect to their global parameters predictions (torque and pressure drop across the rotor), but also looking at the local flow quantities calculations (i.e. the entropy production). Five different rotor geometries have been compared, highlighting the effect of blade thickness and rotor solidity on turbine performance and entropy production.

This manuscript is organized as follows: Section 2 presents the definitions of first- and second-law efficiencies for Wells turbines. Section 3 describes how the intermediate quantities required to evaluate the turbine efficiency can be calculated from CFD results. Section 4 introduces the numerical approach adopted in CFD simulations. Section 5 presents the results obtained under different operating conditions, for several turbulent models, while Section 6 analyses the performance of a number of rotor geometries. Finally, Section 7 draws the conclusions of this work.

2 WELLS TURBINE EFFICIENCY

2.1 First-Law efficiency

Performance of Wells turbines is usually presented, [26], in terms of the following non-dimensional parameters: the flow coefficient ϕ, the torque coefficient $\mathcal{T}^*$, and static or total pressure drop coefficients, p^* and p_t^*, respectively:

$$\phi = \frac{V_a}{\Omega r_{tip}} \qquad \mathcal{T}^* = \frac{\mathcal{T}}{\rho \Omega^2 r_{tip}^5} \qquad p^* = \frac{\Delta p}{\rho \Omega^2 r_{tip}^2} \qquad p_t^* = \frac{\Delta p_t}{\rho \Omega^2 r_{tip}^2} \tag{1}$$

where V_a is the (spatially averaged) axial flow velocity in the turbine duct, ρ the air density (assumed constant and equal to the ambient density), Ω is the angular velocity of the rotor, r_{tip} its tip radius, $\mathcal{T}$ the torque, p and p_t the static and total pressures, and Δ represents the difference between conditions at the 2 sides of the rotor.

The efficiency of a turbine is defined as the ratio between the useful output work and the available energy of the turbine. Two different formulations can be found in the scientific literature for Wells turbines, both entailing an assumption of incompressible flow [27]:

$$\eta_{ad} = \frac{\mathcal{T}\Omega}{\Delta p\, Q} \tag{2}$$

$$\eta_{tt} = \frac{\mathcal{T}\Omega}{\Delta p_t\, Q} \tag{3}$$

Several authors [24, 25, 28] use the formulation in Eqn. (2), as it contains parameters that can be more easily measured in experiments and it is representative of an aerodynamic efficiency of the turbine rotor:

$$\eta_{ad} = \frac{\mathcal{T}\Omega}{\Delta p\, Q} = H \frac{\mathcal{T}/r}{\Delta p \pi \left(r_{tip}^2 - r_{hub}^2\right) V_a/\Omega r} = \frac{X}{Z}\frac{1}{\phi} \tag{4}$$

where X and Z are axial and tangential forces.

Other authors [5, 6, 8, 23, 29] use Eqn. (3). It is the ratio between the rotor useful power and the power for an ideal (isentropic) process between the same initial and final total pressures (i.e. the available power), and it represents a *total-to-total* isentropic efficiency [27].

If the exhaust kinetic energy is entirely wasted, as in case of the Wells turbine [26,30], the *total-to-static* isentropic efficiency definition is more appropriate than the *total-to-total* definition reported in Eqn. (3). Considering the subscripts 1 and 2 for the conditions upstream and downstream the

rotor, respectively, the *total-to-static* efficiency reads as follows [26]:

$$\eta_{ts} = \frac{\mathcal{T}\Omega}{(p_{t1} - p_2)\, Q} \tag{5}$$

Even though this formulation is more representative of the energy conversion process in a Wells turbine, it has (seldom) been adopted both in experimental and numerical analyses and therefore it is not used in the present paper.

2.2 Second-law analysis

In some recent works [10, 12, 13, 21, 22], the efficiency presented in Eqn. (3) has been referred to as *first-law* efficiency, in contrast to a *second-law* efficiency derived from an exergy analysis.

Considering a steady-flow and adiabatic process, the exergy balance for an open system can be written as follows [31]:

$$\dot{E}_{x,in} - \dot{E}_{x,out} = \dot{W} + T_{t,ref}\dot{S}_G \tag{6}$$

where the net exergy flux per unit time ($\dot{E}_{x,in} - \dot{E}_{x,out}$) is equal to the sum of the rate of exergy due to the useful work ($\dot{W}$), and the lost exergy per unit time ($T_{t,ref}\dot{S}_G$). $\dot{S}_G$ represents the entropy generation rate inside the control volume and $T_{t,ref}$ is a reference temperature. A *second-law efficiency* can be defined as the ratio between the useful work and the net exergy flux, i.e.:

$$\eta^{II} = \frac{\dot{W}}{\dot{E}_{x,in} - \dot{E}_{x,out}} = \frac{\dot{W}}{\dot{W} + T_{t,ref}\dot{S}_G} = \frac{\mathcal{T}\Omega}{\mathcal{T}\omega + T_{t,ref}\dot{S}_G} \tag{7}$$

2.3 Linking first- and second-law efficiency

For a machine evolving an ideal gas, the Gibbs' equation integrated between the initial and final total conditions reads:

$$\int_1^2 \mathrm{d}h_t = \int_1^2 \frac{\mathrm{d}p_t}{\rho_t} + \int_1^2 T_t \,\mathrm{d}s \tag{8}$$

The term on the left hand side represents the actual work of the machine, w, the first term on the right hand side is the polytropic work, w_{pol}, and the last term represents the lost work, w_{lost}. Under the assumption of constant heats values and for a turbine:

$$|w| = \frac{|\dot{W}|}{\dot{m}} = -\int_1^2 \mathrm{d}h_t = c_p \left(T_{t1} - T_{t2}\right) \tag{9}$$

$$|w_{pol}| = \frac{|\dot{W}_{pol}|}{\dot{m}} = -\int_1^2 \frac{\mathrm{d}p_t}{\rho_t} \tag{10}$$

$$w_{lost} = \frac{\dot{W}_{lost}}{\dot{m}} = \int_1^2 T_t \,\mathrm{d}s \tag{11}$$

$$|w| = |w_{pol}| - w_{lost} \tag{12}$$

We can also define an isentropic work, referring to a transformation at constant entropy between the initial and final total pressures

$$|w_{is}| = \frac{|\dot{W}_{is}|}{\dot{m}} = -\int_1^{2_{is}} \mathrm{d}h_t = c_p \left(T_{t1} - T_{t2,is}\right) \tag{13}$$

Figure 2 reports graphically the difference between polytropic, isentropic, actual and lost specific works for a machine evolving a compressible flow.

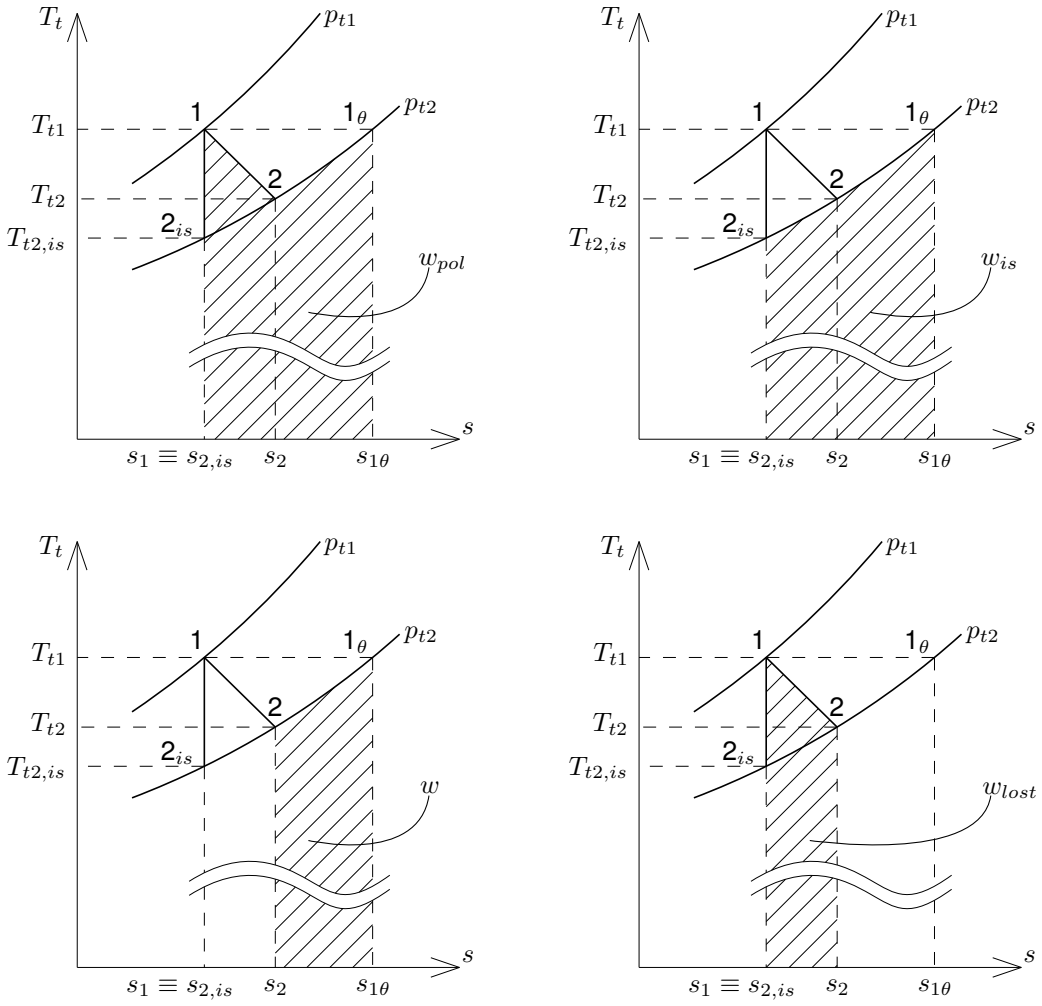

Fig. 2. Representation of specific works on the $T_t - s$ plane

The isentropic work represents the maximum work that a turbine can exchange with the fluid (i.e. the available energy per unit time), while the polytropic work is the sum of actual work and lost work (due to friction). In a turbine, the polytropic work is always greater than the isentropic work, with the difference being the heating work gain [27].

$$|w_{pol}| = |w| + w_{lost} > |w_{is}| \tag{14}$$

Conversely, the isentropic efficiency $\eta_{is} = {}^{|w|}/_{|w_{is}|}$ is always greater than the polytropic effi-

ciency $\eta_{pol} = {|w|}/{|w_{pol}|}$. The latter is more representative of the inefficiencies in turbomachine, as it does not take into account the heating work gain and only considers the lost work.

For low pressure ratio machines (as in the case of Wells turbine) $(T_{t1} - T_{t2,is}) \ll T_{t1}$ and the following approximations can be made:

$$w_{pol} \approx w_{is} \implies \eta_{pol} \approx \eta_{is} \tag{15}$$

$$\int_1^2 T_t \, \mathrm{d}s \approx T_{t,ref} \, (s_2 - s_1) \tag{16}$$

provided that $T_{t,ref}$ is chosen appropriately (i.e. in the range of temperatures involved in the transformation). Under these assumptions

$$|w| \approx |w_{pol}| - T_{t,ref} \, (s_2 - s_1) \tag{17}$$

In terms of powers, observing that for low speed flows ρ_t can be approximated with the static density, ρ, one has:

$$|\dot{W}_{pol}| = \dot{m} \, |w_{pol}| = -\dot{m} \int_1^2 \frac{\mathrm{d}p_t}{\rho_t} \approx \frac{\dot{m}}{\rho_t} \, (p_{t1} - p_{t2}) \tag{18}$$

$$\dot{W}_{lost} = \dot{m} \, w_{lost} = \dot{m} \int_1^2 T_t \mathrm{d}s \approx \dot{m} T_{t,ref} \, (s_2 - s_1) \tag{19}$$

$$|\dot{W}| = \dot{m} \, |w| = -\dot{m} \int_1^2 \mathrm{d}h_t = \dot{m} c_p \, (T_{t1} - T_{t2}) = \mathcal{T}\Omega \tag{20}$$

In addition, the lost work can be written in terms of the entropy generated inside the domain,

following Gauss' divergence theorem [32]:

$$\dot{m}T_{t,ref}(s_2 - s_1) = T_{t,ref}\int_{CV}\rho\sigma\,\mathrm{d}\mathcal{V} = T_{t,ref}\dot{S}_G \tag{21}$$

where $\sigma = \mathrm{d}s_{\mathcal{V}}/\mathrm{d}t$ represents the entropy generation rate per unit mass, and CV a control volume enclosing the turbine.

Putting together Eqns. (18), (19) and (20) with the definitions of first- and second-law efficiencies, Eqns. (3) and (7), it follows that:

$$\eta^{II} = \frac{\mathcal{T}\Omega}{\mathcal{T}\Omega + T_{t,ref}\dot{S}_G} \approx \frac{\mathcal{T}\Omega}{\Delta p_t Q} = \eta_{tt} \tag{22}$$

Equation (22) is a direct consequence of the equivalence of polytropic and isentropic work for a low pressure ratio process. In light of the growing interest in evaluating the performance of Wells turbines with the second-law efficiency, the validity of this approximation will be verified in this paper with several turbulence models and for different Wells turbine rotors.

3 ENTROPY CALCULATION FROM CFD (RANS) SIMULATIONS

The quantities required to estimate the efficiency of a Wells turbine can be calculated using numerical simulations, i.e. by solving the governing Navier-Stokes (NS) equations numerically. These quantities include the turbine torque $\mathcal{T}$, the static and total pressure drops Δp and Δp_t, the volumetric flow rate Q, and the entropy generation rate $\dot{S}_G$.

As a Direct Numerical Simulation (DNS) of the NS equations for most flows of industrial interest is still beyond the capability of current computers, the most common and practical approach is the solution of the Reynolds Averaged Navier-Stokes (RANS) equations, which are derived by replacing the instantaneous flow variables in the NS with the sum of a mean value and a fluctuating component with zero mean value ($\varphi = \overline{\varphi} + \varphi'$).

For a compressible flow, assuming negligible heat transfer as common in turbomachinery appli-

cations, the RANS equations of conservation of mass, momentum and energy read as follows [33]:

$$\begin{cases} \dfrac{\partial \overline{\rho}}{\partial t} + \nabla \cdot \left(\overline{\rho} \overline{\mathbf{V}} \right) = 0 \\ \dfrac{\partial \overline{\rho} \overline{\mathbf{V}}}{\partial t} + \nabla \cdot \left(\overline{\rho} \overline{\mathbf{V}} \otimes \overline{\mathbf{V}} + \overline{\rho \mathbf{V}' \otimes \mathbf{V}'} \right) = -\nabla \overline{p} + \nabla \cdot \overline{\mathbf{\Pi}} \\ \dfrac{\partial \overline{\rho} \overline{h}}{\partial t} + \nabla \cdot \left(\overline{\rho} \overline{\mathbf{V}} \, \overline{h} \right) = \dfrac{D \overline{p}}{D t} + \overline{\mathbf{\Pi}} : \nabla \overline{\mathbf{V}} + \overline{\mathbf{\Pi}' : \nabla \mathbf{V}'} \end{cases} \tag{23}$$

where $\mathbf{V}$ is the velocity vector, h is the static enthalpy, and $\mathbf{\Pi}$ is the deviatoric stress tensor, that for a Newtonian flow can be expressed as the sum of the contributions due to the strain rate tensor $\nabla^S \mathbf{V}$ and the volumetric tensor $(\nabla \cdot \mathbf{V}) \, \mathbf{I}$, each one multiplied by a constant, i.e. the molecular viscosity μ and the bulk viscosity λ, respectively.

$$\mathbf{\Pi} = \mu \left(\nabla \mathbf{V} + \nabla \mathbf{V}^T \right) + \lambda \left(\nabla \, \mathbf{V} \right) \mathbf{I} = 2 \mu \nabla^S \mathbf{V} + \lambda \left(\nabla \cdot \mathbf{V} \right) \mathbf{I} \tag{24}$$

In Eqn. (23), the prime symbol denotes fluctuating quantities, and the overbar denotes time-averaged flow quantities. Density fluctuations, i.e. ρ', have been neglected as they start to affect turbulence around a Mach number of 1 [34]. In the presence of significant density fluctuations, the Favre-averaged NS equations can be used instead [35].

The terms which represent the effects of turbulent fluctuations on the mean flow are not resolved by the RANS approach and need to be modeled to allow the solution of the system of equations. The turbine torque $\mathcal{T}$ can then be calculated by integrating pressure and viscous stresses on the turbine blade, while the pressure drops require the evaluation of the (mass-flow) averaged pressure on surfaces appropriately defined upstream and downstream of the turbine. The evaluation of the entropy generation rate $\dot{S}_G$ requires more attention, as an entropy equation is not generally solved in CFD programs, as it would make the system of equations in Eqn. (23) overdetermined. An entropy equation can be derived by linking Gibbs' relation with the momentum

and energy equations, as described in [32, 36]:

$$\frac{\partial \overline{\rho}\,\overline{s}}{\partial t} + \nabla \cdot \left(\overline{\rho}\overline{\mathbf{V}}\overline{s}\right) + \nabla \cdot \left(\overline{\rho}\overline{\mathbf{V}'s'}\right) = \overline{\rho}\sigma_{V,mf} + \overline{\rho}\,\overline{\sigma_{V,T}} \tag{25}$$

where the right hand side represents the entropy production rate per unit mass due to fluid flow: in particular, $\sigma_{V,mf}$ is the contribution due to the mean flow and $\overline{\sigma_{V,T}}$ is the one due to turbulent fluctuations. The two terms on the right hand side of Eqn. (25) are defined as follows, neglecting the effect of temperature fluctuations on viscous entropy production as in [36, 37]:

$$\overline{\rho}\,\sigma_{V,mf} = \frac{1}{\overline{T}}\left(\overline{\mathbf{\Pi}} : \nabla\overline{\mathbf{V}}\right) \tag{26}$$

$$\overline{\rho}\,\overline{\sigma_{V,T}} = \frac{1}{\overline{T}}\left(\overline{\mathbf{\Pi}' : \nabla\mathbf{V}'}\right) \tag{27}$$

Only the terms containing mean quantities are solved (and hence available) in a RANS approach. All terms involving fluctuating quantities ($\overline{\rho}\overline{\mathbf{V}' \otimes \mathbf{V}'}$ and $\overline{\mathbf{\Pi}' : \nabla\mathbf{V}'}$) need to be modeled. The most common approaches are Linear Eddy Viscosity models, based on the so-called Boussinesq's hypothesis:

$$-\overline{\rho}\overline{\mathbf{V}' \otimes \mathbf{V}'} = \mathbf{\Pi}_R = \mu_T\left(\nabla\overline{\mathbf{V}} + \nabla\overline{\mathbf{V}}^T\right) - \frac{2}{3}\overline{\rho}k\mathbf{I} = 2\mu_T\nabla^S\overline{\mathbf{V}} - \frac{2}{3}\overline{\rho}k\mathbf{I} \tag{28}$$

where $\mathbf{\Pi}_R$ is the Reynolds' stress tensor, μ_T is the turbulent viscosity and k is the turbulent kinetic energy per unit mass ($k = \frac{1}{2}(-\overline{\rho}\overline{u'^2} - \overline{\rho}\overline{v'^2} - \overline{\rho}\overline{w'^2})$). The term μ_t is usually modeled adding additional transport equations. The quantity $\left(\overline{\mathbf{\Pi}' : \nabla\mathbf{V}'}\right)$ represents the dissipation of turbulent kinetic energy into heat and is usually referred to with the symbol ε. Finally, the global entropy generation per

unit time ($\dot{S}_G$) can be estimated by integrating the viscous dissipation in the domain of interest:

$$\dot{S}_G = \int_{CV} \overline{\rho} \left(\sigma_{V,mf} + \overline{\sigma_{V,T}} \right) d\mathcal{V} \tag{29}$$

This approach for the calculation of entropy production is referred to as a *direct* method in [36]. Alternatively, the same authors suggested the use of an *indirect* method, which is derived from the equation of conservation of entropy (Eqn. (25)), neglecting turbulent convection and diffusion across the boundaries, and integrating in an appropriate control volume CV.

$$\dot{S}_G \approx \int_A \overline{\rho}\,\overline{s}\overline{\mathbf{V}} \cdot \mathbf{n} dA + \frac{\partial}{\partial t} \int_{CV} \overline{\rho}\,\overline{s} d\mathcal{V} \tag{30}$$

In Eqn. (30), A represents the boundary of the control volume CV, and s the specific entropy which can be evaluated under the assumption of ideal gas, as recalled in Sec. 2.3.

3.1 Evaluation of entropy production with different turbulence models

As mentioned in the previous section, turbulent quantities are not directly available in RANS approaches and need to be modeled. Different turbulence closure methods are available in CFD solvers, the most common being the ones based on the so-called Boussinesq's hypothesis, which assumes a linear dependency between Reynolds' stress and strain tensors (Eqn. (28)). The most famous ones are $k-\varepsilon$ and $k-\omega$ models, which derive the turbulent viscosity μ_T based on two additional partial differential equations, for turbulent kinetic energy (k) and its rate of dissipation (ε), and for k and its specific dissipation rate (ω), respectively. Of particular interest for this work is the equation of conservation for the turbulent kinetic energy, which is reported in Eqn. (31):

$$\frac{\partial \overline{\rho} k}{\partial t} + \nabla \cdot \left(\overline{\rho} k \overline{\mathbf{V}} \right) = \nabla \cdot \left(-\overline{p' \mathbf{V}'} + \overline{\mathbf{\Pi}' \cdot \mathbf{V}'} - \frac{1}{2} \overline{\rho} \overline{\mathbf{V}' \cdot \mathbf{V}' \otimes \mathbf{V}'} \right) - \overline{\mathbf{\Pi}' : \nabla \mathbf{V}'} - \overline{\rho} \overline{\mathbf{V}' \otimes \mathbf{V}'} : \nabla^S \overline{\mathbf{V}} \tag{31}$$

where the last two terms on the right hand side of the equation represent the rates of dissipation and production of k, respectively. The former, referred to with the symbol ε, is present also in the energy equation (Eqn. (23)), as the dissipated turbulent kinetic energy is transformed into heat. The production of k can be expressed following the Boussinesq's hypothesis in Eqn. (28):

$$\overline{\mathbf{\Pi}' : \nabla \mathbf{V}'} = \overline{\rho}\varepsilon \tag{32}$$

$$-\overline{\rho}\overline{\mathbf{V}' \otimes \mathbf{V}'} : \nabla^S \overline{\mathbf{V}} = 2\mu_T \left(\nabla^S \overline{\mathbf{V}}\right)^2 - \frac{2}{3}\overline{\rho}k \left(\nabla \cdot \overline{\mathbf{V}}\right) \tag{33}$$

Using Eqn. (32), the viscous dissipation in Eqn. (26) and (27) can be calculated as follows:

$$\overline{T\sigma_V} = \overline{T}\sigma_{V,mf} + \overline{T\sigma_{V,T}} = \frac{1}{\overline{\rho}}\left(\overline{\mathbf{\Pi}} : \nabla \overline{\mathbf{V}} + \overline{\mathbf{\Pi}' : \nabla \mathbf{V}'}\right) = \frac{1}{\overline{\rho}}\left(2\mu \left(\nabla^S \overline{\mathbf{V}}\right)^2 + \lambda \left(\nabla \cdot \overline{\mathbf{V}}\right)^2 + \overline{\rho}\varepsilon\right) \tag{34}$$

Many authors [38–40], assuming a local equilibrium between turbulent entropy production and dissipation, i.e. $\overline{\rho}\varepsilon = 2\mu_T \left(\nabla^S \overline{\mathbf{V}}\right)^2 - \frac{2}{3}\overline{\rho}k \left(\nabla \cdot \overline{\mathbf{V}}\right)$, introduce the following approximation:

$$\overline{T\sigma_V} = \frac{1}{\overline{\rho}}\left[2\left(\mu + \mu_T\right)\left(\nabla^S \overline{\mathbf{V}}\right)^2 + \left(\lambda \nabla \cdot \overline{\mathbf{V}} - \frac{2}{3}\overline{\rho}k\right)\left(\nabla \cdot \overline{\mathbf{V}}\right)\right] \tag{35}$$

The last two expressions (Eqns. (34) and (35)) are alternative methods for calculating the entropy production due to viscous dissipation per unit mass, and the choice between the two methodologies depends on the selected turbulence closure model:

1. In $k-\varepsilon$ and $k-\omega$ models, both approaches can be adopted because in the former ε is directly available, while in the latter it can be calculated as a function of the turbulent kinetic energy k and specific dissipation rate ω, i.e. $\varepsilon = \omega k \beta^*$, where β^* is a model constant which depends on the specific implementation. An important consideration has been proposed in [39], where the authors note that the second approach (Eqn. (34)) is more reliable, because in RANS

approaches ε is only used as an intermediate quantity to calculate μ_t and $\mathbf{\Pi}_R$, which interact with the mean flow through the momentum and energy equations.

2. In Spalart-Allmaras (S-A) models only the second approach can be used, as the method solves directly a transport equation for kinematic eddy viscosity $\tilde{\nu}$, which is related to μ_T through the following expressions:

$$\mu_T = \overline{\rho}\tilde{\nu} f_{v1}; \quad f_{v1} = \frac{\left(\tilde{\nu}/\nu\right)^3}{\left(\tilde{\nu}/\nu\right)^3 + C_{v1}^3} \tag{36}$$

where f_{v1} is the viscous damping function. In addition to the standard formulation of the $k-\varepsilon$ model, the Realizable (REAL) $k-\varepsilon$ formulation has also been considered. It is a newer implementation [41] that differs from the original for a new formulation of the turbulent viscosity and a new transport equation for the dissipation rate ε. The Fluent® User's Guide [42] states that the $k-\varepsilon$ REAL model provides superior performance for flows involving rotation, boundary layers under strong adverse pressure gradients, separation and recirculation.

4 METHODOLOGY

The turbine geometry and operating conditions simulated in this work are the ones presented in the experimental work from Setoguchi *et al.* [43]. The main details are summarized in Table 1.

The domain for the numerical simulations is reported in Figure 3 (a): it is a straight duct representing a single blade passage of the turbine, with periodic boundary conditions at the 2 sides. Simulating a single passage of a tubomachinery's blade row (or even multiple single passages from different blade rows, with an appropriate treatment of the inter-row interface) is a common practice in turbomachinery RANS simulations [44–46] when the hypothesis of periodic flow with respect to the blade pitch is valid, i.e. in the absence of flow structures larger than the blade pitch. This approximation has been often used in Wells turbine simulations [8, 9, 21, 47] . The interaction bewtween stationary and moving parts has been modeled using a "frozen rotor approach", also referred to as the "multiple reference frame" (MRF) model in the Fluent User's Guide [42]. The model can be used for turbomachinery applications in which rotor-stator interaction is rel-

Table 1. Geometric and operating data

rotor tip diameter [mm]	300
rotor hub diameter [mm]	210
tip clearance [mm]	1
chord length [mm]	90
sweep ratio [-]	0.417
number of blades [-]	5 - 6 - 7
blade profiles	NACA0012 - NACA0015 - NACA0020
solidity at tip radius [-]	0.48 - 0.57 - 0.67
rotational speed [rpm]	2500
operating frequency [s^{-1}]	1/6
non-dimensional frequency $(\pi f c)/U$[-]	1.2×10^{-3}
Reynolds' number [-]	2×10^5 (based on rotor tip radius and chord length)

atively weak, and the flow is relatively uncomplicated at the interface between the moving and stationary zones. This seems to be a good approximation for the present case study, where the interaction between moving parts is only at the hub and casing of the duct where the turbine is housed. The same model has been used in the majority of previous CFD analyses of Wells turbines [9, 13, 21, 48–51]. The OWC chamber is not included in the domain (as done for example in [52–54]), because its main effect is to cause a delay between the movement of the water level in the chamber and the mass-flow in the turbine duct, without significant modifications to the turbine performance.

Uniform inlet boundary conditions have been used for velocity, total temperature and turbulent quantities. The velocity has been set to a value, fixed in steady simulations and sinusoidally variable in time in dynamic simulations, chosen to obtain the required value or range of flow coefficients (see Eqn. 1). Figure 4 shows a typical variation of flow coefficient ϕ, where T_w represents the wave period. The inlet total temperature has been set to 288 K and the turbulent quantities are calculated by the solver based on the values set for turbulent intensity and length scale (2% and 7% of the blade height, as suggested in [42]). An uniform value of static pressure has been specified at the outlet, while periodic boundary conditions have been used at the two sides of the

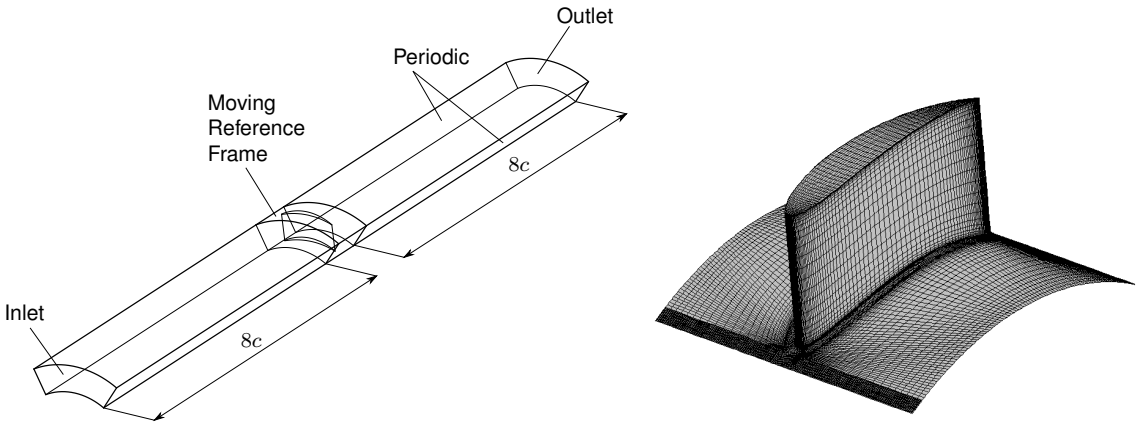

(a) Computational domain (b) Blade and hub mesh

Fig. 3. Computational domain and mesh for simulations

passage of the computational domain (Figure 3). Inlet and outlet are inverted for negative values of the flow coefficient. A multi-block structured grid has been used to discretize the volume, with a C-grid around the blade able to capture the boundary layer flow and an H-grid in the rest of domain, see Fig. 3 (b).

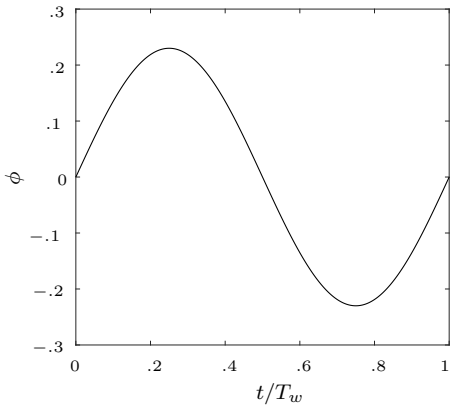

Fig. 4. Inlet boundary condition for dynamic simulations, in terms of flow coeffcient ϕ

Four different turbulence closure models have been compared: the $k-\omega$ SST, the standard (STD) and realizable (REAL) $k-\varepsilon$ and the Spalart-Allmaras (S-A) models. Numerical simulations have been conducted using the commercial CFD software Ansys Fluent® 17.0. The SIMPLEC algorithm has been used for the pressure-velocity coupling, a second-order centered scheme for

pressure and viscous terms and a second-order upwind scheme for convective terms. Multiple reference frames have been adopted to simulate the interaction between stationary and rotating volumes. Steady simulations have been run with a time-dependent approach (and constant boundary condition) with a time step of 10^{-4} until convergence of the monitored quantities (torque and pressure drops) were obtained (within 0.1% in the last 1000 time steps), while time dependent simulations were run for 3 wave periods, with a time step sufficient to obtain results independent from the temporal discretization. Results from the last 2 periods differed always by less than 0.1%, hence periodic convergence has been considered achieved. A first-order implicit temporal discretization approach was used, with 5 sub-iterations per time step. The default settings of Ansys Fluent have been maintained: at every sub-iteration, 2 sweeps of the algebraic multigrid with a maximum of 40 levels are allowed, with the Gauss-Seidel smoother. An explicit convergence criterion was not set in time-dependent simulations, but rather the number of sub-iterations was kept fixed, and the time step size reduced until results were independent from its value. Maximum residuals were found to be of the order of 10^{-4} for appropriate values of the time step. Increasing the number of sub-iterations would have achieved the same effect, at least to a certain time step size, as shown in [55].

All simulations were run on dual processor 3.30 GHz 8 core Intel Xeon E5-2667 v2 CPUs. Each time step required about 3 seconds, and complete periodic simulations required as long as 3 months.

4.1 Verification and validation

The choice of the spatial discretization has been made following a grid convergence study: Fig. 5 reports the results obtained for the non-dimensional coefficients of torque and pressure drop using 3 grid sizes (about 1, 2, and 3 millions cells, respectively) and a non-dimensional wall distance (y^+) below unity, for the turbine with the highest number of blades ($z = 7$, i.e. with a rotor tip solidity equal to 0.67) and NACA0020 profile, where the largest gradients of flow quantities are expected. The $k - \omega$ SST model has been used for verification. Minor differences are present between the coarser grid and the finest 2 grids, the results of which appear indistinguishable, at least in the range of flow coefficients of importance for this study. As a consequence, the medium

mesh (about 2 million cells) has been selected. Experimental data are also reported, and present the famous hysteretic loop due to the capacitive effect of the OWC chamber [52, 54, 56], which is not included in the current simulations. Numerical results lie in the middle of the hysteresis loop, therefore attesting the appropriateness of the numerical results.

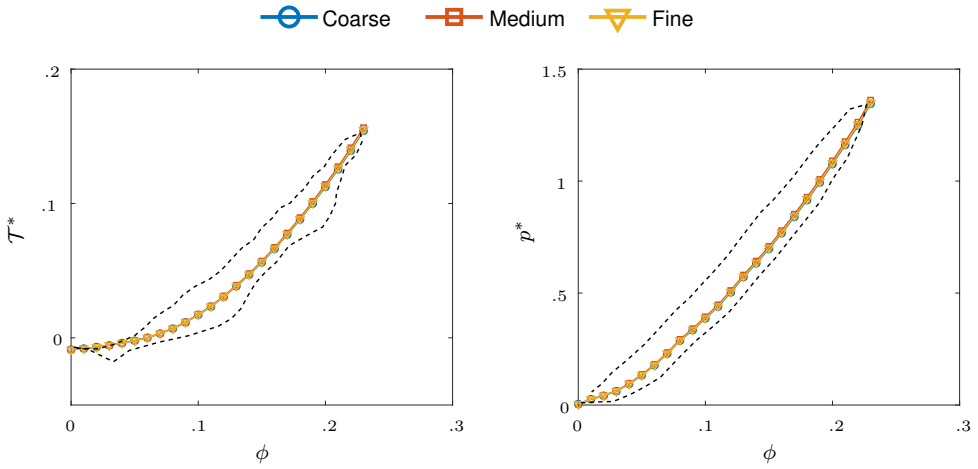

(a) Non-dimensional torque (b) Non-dimensional static pressure drop

Fig. 5. Verification of the spatial discretization using three different grid sizes

Fig. 6 reports the effect of the time step size on the torque and the entropy generation coefficients. Five time step values have been compared running 3 periods of oscillation, with an amplitude for the sinusoidal inlet velocity appropriate to produce a maximum flow coefficient ϕ of 0.23, as in the experiment [43]. Only the last period is reported, for brevity. The non-dimensional entropy generation has been evaluated using both the dissipation and the generation of turbulent kinetic energy (as explained in Section 3), and the results have been expressed in non-dimensional form, as follows:

$$K_{\dot{S},d} = \frac{\int_{CV} \left(2\mu \left(\nabla^S \overline{\mathbf{V}} \right)^2 + \lambda \left(\nabla \cdot \overline{\mathbf{V}} \right)^2 + \overline{\rho}\varepsilon \right) dV}{\frac{1}{2}\rho_{in}\Omega^3 r_{tip}^5} \tag{37}$$

$$K_{\dot{S},g} = \frac{\int_{CV} \left[2\left(\mu + \mu_T\right) \left(\nabla^S \overline{\mathbf{V}} \right)^2 + \left(\lambda \nabla \cdot \overline{\mathbf{V}} - \frac{2}{3}\overline{\rho}k \right) \left(\nabla \cdot \overline{\mathbf{V}} \right) \right] dV}{\frac{1}{2}\rho_{in}\Omega^3 r_{tip}^5} \tag{38}$$

where $K_{\dot{S},d}$ is the non-dimensional entropy production rate in the control volume, evaluated using the turbulent kinetic energy dissipation defined in Eqn. (34), and $K_{\dot{S},g}$ is the non-dimensional entropy production rate in the control volume, evaluated using the turbulent kinetic energy generation defined in Eqn. (35). It should be noted that in the presence of an incompressible flow, the second term in the round brackets of Eqn. (37) and the last term in the square brackets of Eqn. (38) are null. In the current analyses, given the low relative Mach number in the vicinity of the blade (about 0.3) these terms never accounted for more than 0.02% of the total entropy production. The authors preferred to treat the flow as compressible for generality, as the derivation in the current form can be applied also for higher Mach number machines [57, 58].

The analysis highlights how time steps larger than $T_w/16000 \approx 4 \times 10^{-4}$ s produce spurious phase errors [59], which manifest in a false delay, previously erroneously interpreted as an aerodynamic hysteresis of the turbine [52, 54, 56, 60]. This effect is reported in Figure 6, where it is evident how hysteretic effects disappear when sufficiently small time step sizes are used (below $T_w/16000 \approx 410^{-4}$ s). Reducing the time-step size has a similar effect to increasing the number of sub-iterations: [55] have shown how it is the total number of sub-iterations per cycle (i.e number of time steps per cycle times number of sub-iterations per time step) that influences the temporal convergence. For the selected grid and working conditions, the maximum value of the Courant number (CFL) is proportional to the time step size and ranges from 6400 (for $dt = T_w/1000$) to 25 (for $dt = T_w/256000$). Performance during inflow (negative flow coefficients) and outflow (positive flow coefficients) does not present significant differences. The absence of dynamic effects is in agreement with the large literature on oscillating lifting surfaces [61–63], where significantly larger non-dimensional frequencies are required to produce an appreciable hysteresis [64, 65].

A similar analysis, Fig. 7, has been conducted in the presence of a temporal profile for the inlet velocity with a larger amplitude ($\phi_{max} = 0.325$), sufficient to lead to blade stall. The results of the analysis show how an even smaller temporal discretization is required to achieve results independent from the time step (about $1.25E-5$ s), with a corresponding value of the maximum CFL of about 12.5. In the presence of stall, a small hysteretic loop is present, which is caused by the fact that the boundary layer reattaches to the blade surface for a flow coefficient (and therefore

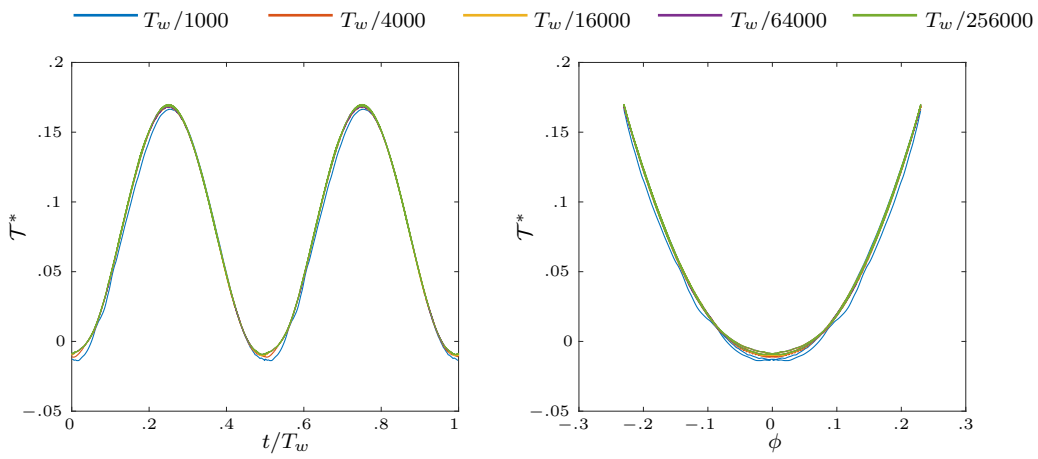

(a) Non-dimensional torque history (final period)

(b) Non-dimensional torque as a function of the flow coefficient

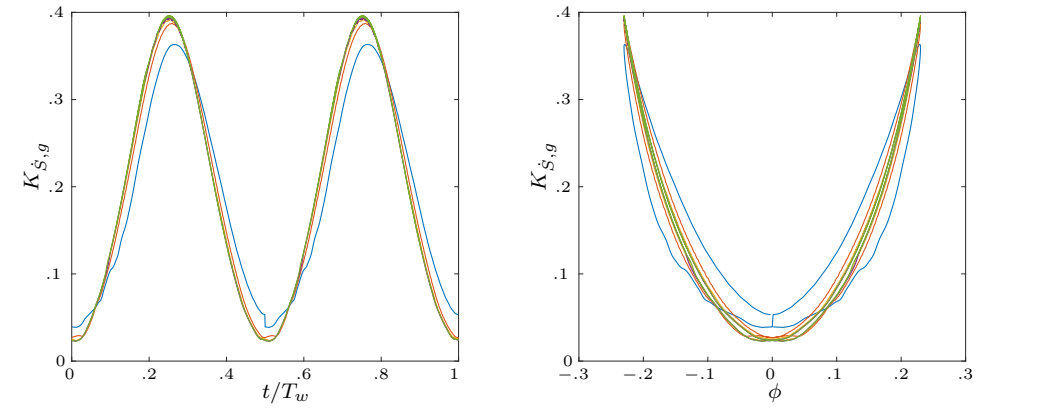

(c) Non-dimensional entropy generation (final period)

(d) Non-dimensional entropy generation as a function of the flow coefficient

Fig. 6. Verification of the temporal discretization using five different time step sizes with a maximum flow coefficient $\phi_{max} = 0.23$

an angle of attack) smaller than the one leading to stall during the acceleration phase. This phenomenon is not necessarily linked to the dynamic operating conditions, as a static stall hysteresis is documented for many lifting surfaces [66, 67], while significantly larger non-dimensional frequencies are required to produce appreciable effects on the performance [62, 63]. In any case, the value of the performance parameters after reattachment, during deceleration, is indistinguishable from the one attained during acceleration.

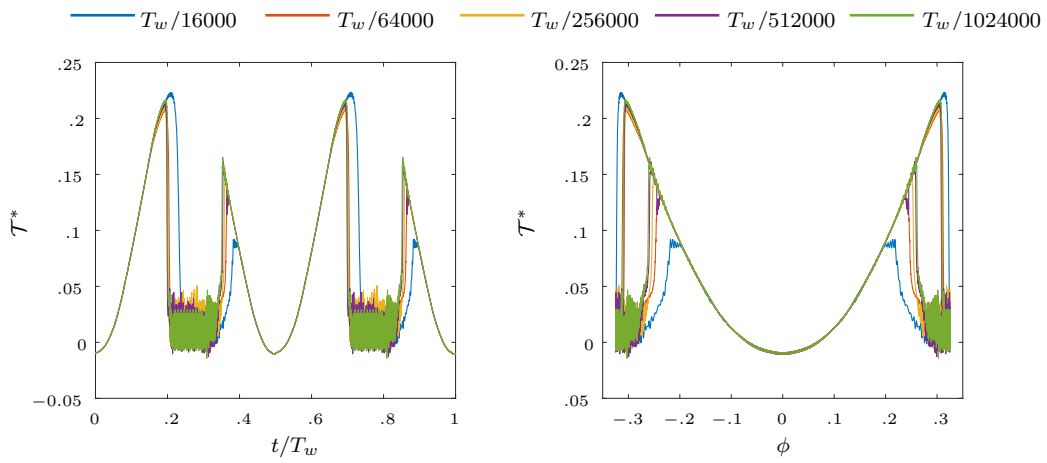

(a) Non-dimensional torque history (final period)

(b) Non-dimensional torque as a function of the flow coefficient

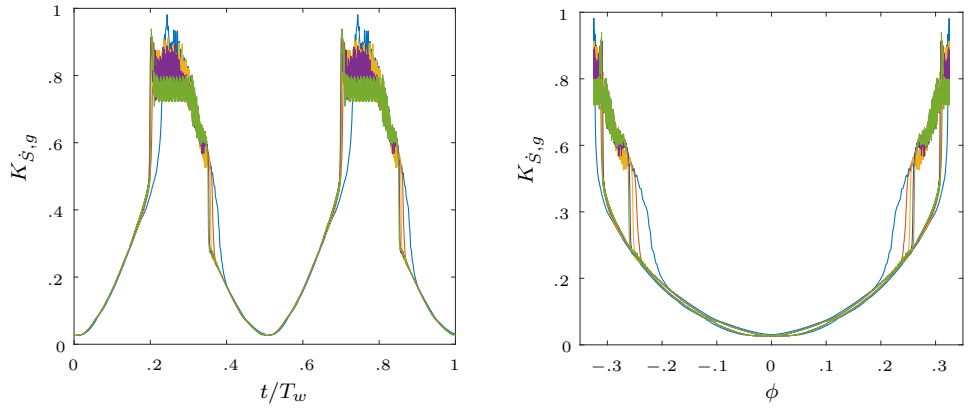

(c) Non-dimensional entropy generation (final period)

(d) Non-dimensional entropy generation as a function of the flow coefficient

Fig. 7. Verification of the temporal discretization using five different time step sizes with a maximum flow coefficient $\phi_{max} = 0.325$

5 RESULTS - COMPARISON AMONG DIFFERENT TURBULENCE MODELS

In this paragraph, simulations with different turbulence models are reported for the same rotor geometry, i.e. the rotor with 6 blades (rotor tip solidity equal to 0.57) and NACA0015 blade profile. Two periodic operating conditions have been simulated: one with a maximum flow coefficient $\phi_{max} = 0.23$, not sufficient to produce stall, and one with a $\phi_{max} = 0.345$, enough to cause deep stall of the rotor at least with some turbulence models.

5.1 Simulations with $\phi_{max} = 0.23$

Fig. 8 reports the non-dimensional parameters commonly adopted in Wells turbines characterization with respect to the flow coefficient, as calculated in Eqn. (1). Positive values of the flow coefficient refer to the outflow, while negative ones refer to the inflow phase.

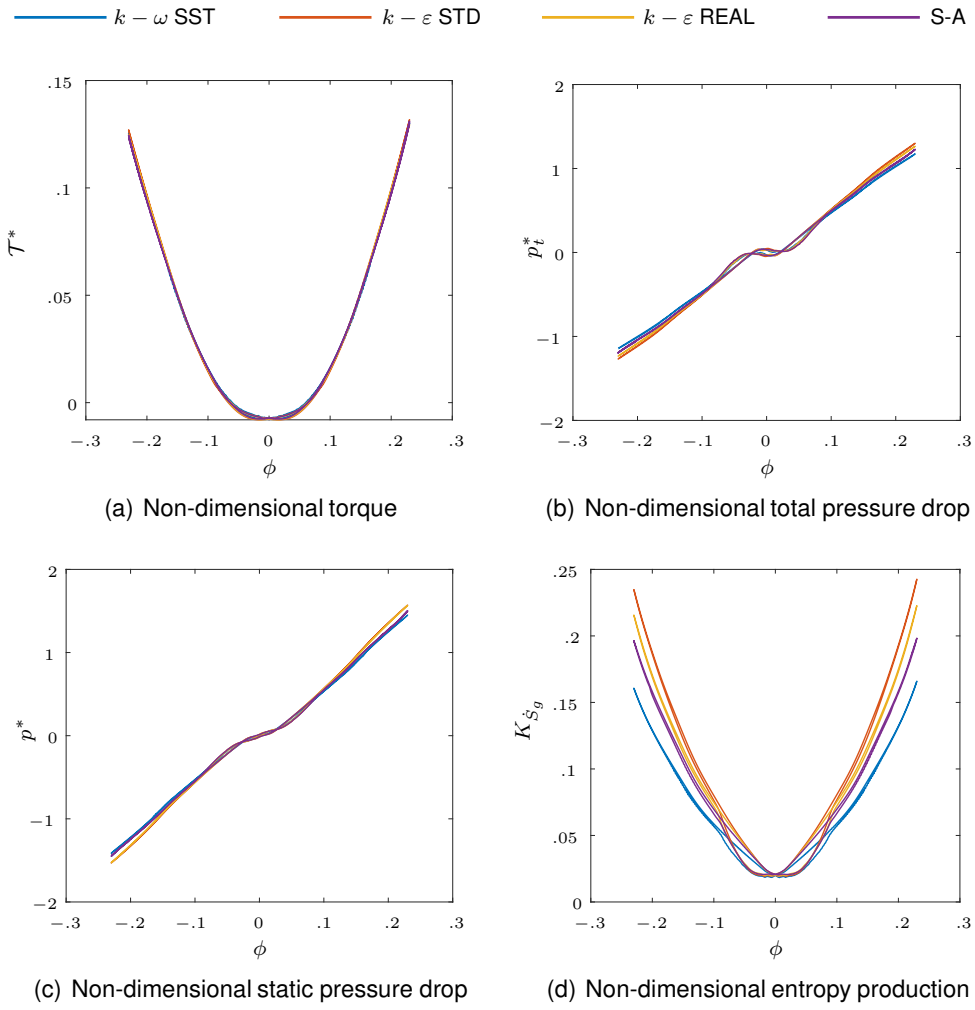

(a) Non-dimensional torque

(b) Non-dimensional total pressure drop

(c) Non-dimensional static pressure drop

(d) Non-dimensional entropy production

Fig. 8. Non-dimensional performance of the rotor with NACA0015 blade profile and $z = 6$ as a function of flow coefficient ϕ estimated with different turbulence closure models

Using different turbulence models does not affect the prediction of the rotor performance and their estimated trends are substantially overlapping (see Fig. 8) and matching the experimental data as reported in Fig. 5. A small overprediction of the pressure coefficients, i.e. p_t^* and p^*, can

be observed in the simulations made with the $k-\varepsilon$ models, while the comparison of $k-\omega$ and S-A does not highlight differences. The torque is well predicted by all models, and no significant differences can be observed.

On the contrary, the non-dimensional entropy generation, Fig. 8(d), shows different values depending on the turbulence model selected. In particular, $k-\varepsilon$ models estimate a higher entropy production with respect to the other models. In order to better understand these large differences, the entropy generation calculations have been reported in Fig. 10: the mean values over a cycle of both $K_{\dot{S},d}$ and $K_{\dot{S},g}$ (defined in Eqns. (37) and (38)) are reported, for two different control volumes, a smaller one going from half a chord upstream to half a chord downstream of the rotor (A), and a larger one enclosing all computational domain (B) (8 chords upstream and downstream of the rotor), as indicated in Fig 9. The results from control volume A are reported in Fig. 10 (a), the results from control volume B are reported in Fig. 10 (b).

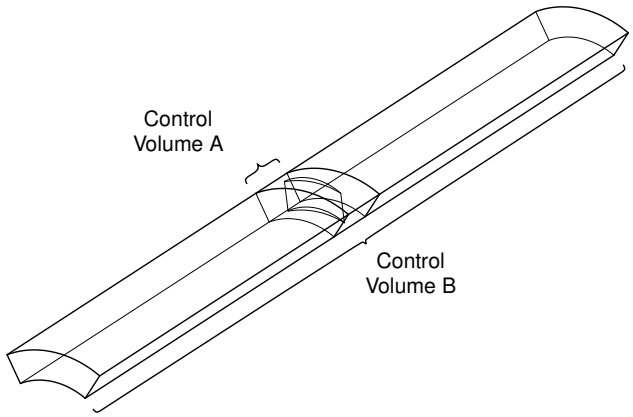

Fig. 9. Schematic view of the control volumes in which are made the entropy production calculations

From the results presented in Fig. 10, the evaluation of the (non-dimensional) entropy production using the generation and dissipation of turbulent kinetic energy leads to the same results only if the calculation is made in a large enough control volume (control volume B), while an appreciable difference exists when the boundaries of the control volume are too close to the rotor (control volume A), mainly due to the neglection of the wake, where the turbulent energy dissipation is larger than its production. In the Spalart-Allmaras model, as explained in Section 3.1, only the

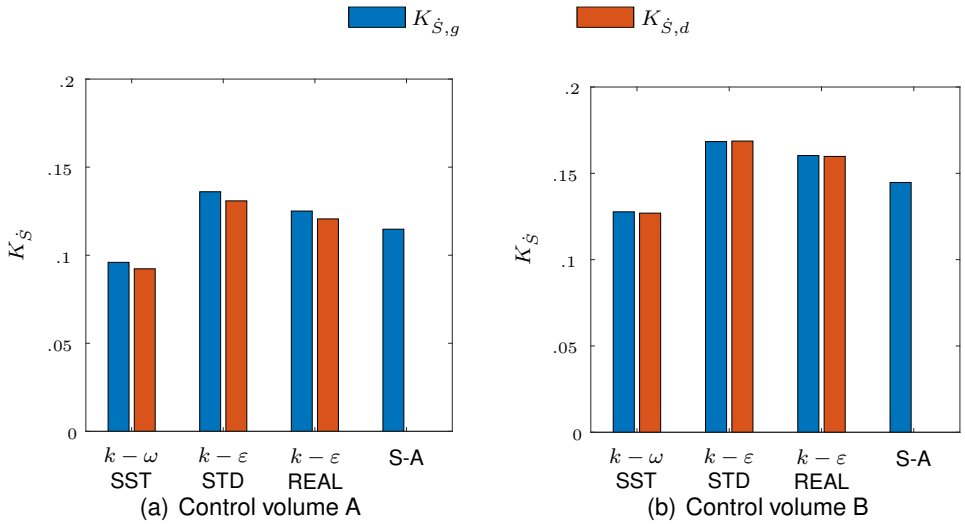

Fig. 10. Mean non-dimensional entropy production rate evaluated in a smaller (a) and larger (b) control volume

production of turbulent kinetic energy is available.

Even more interesting it is to observe the differences between the turbulence models selected for this study. The $k-\epsilon$ models predict an entropy generation rate significantly larger than the $k-\omega$ model, by about 30%, in the larger control volume. The Spalart-Allmaras prediction is lower, but still larger than the one given by the $k-\omega$ model, by about 15%. This is due to the different formulation of the turbulent kinetic energy production and destruction terms, which are strictly related to the entropy production, as shown in Sec. 3. The $k-\omega$ SST models, in particular, uses a damping function in the boundary layer which is particularly effective in the presence of low Reynolds number flows, as in this case [68, 69]. This has an effect both on the amount of entropy generated, but also on the capability of the model to predict flow separation and stall at low Reynolds numbers.

Fig. 11 reports the total exergy in a cycle of period T_w, defined in Eqn. (6), using 3 approaches,

which, as explained in Section 2.3, should in theory lead to very similar results.

$$
\begin{aligned}
E_P &= \int_{T_w} \Delta p_t Q \, dt \\
E_E &= \int_{T_w} \left(\dot{m} c_p \Delta T_t - \dot{m} T_{t,ref} \Delta s \right) dt \\
E_S &= \int_{T_w} \left(\mathcal{T} \Omega + T_{t,ref} \dot{S}_G \right) dt
\end{aligned}
\tag{39}
$$

The last 2 methods are the *indirect* and *direct* approaches described by Herwig [36]. The exergy calculation E_S has been evaluated both considering the generation, $E_{S,g}$, and dissipation, $E_{S,d}$, of turbulent kinetic energy (Eqns. (37) and (38)).

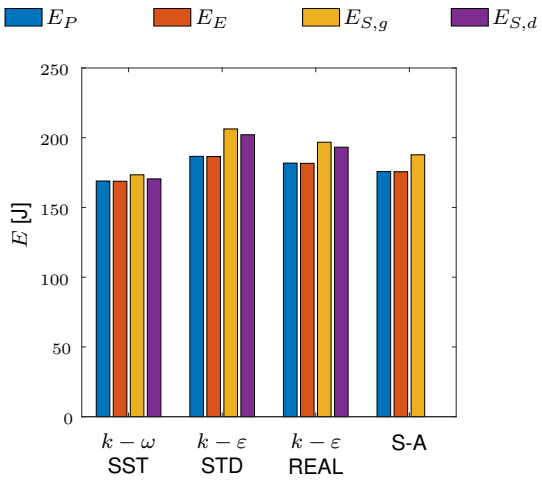

Fig. 11. Total exergy calculations averaged on a cycle for different turbulence closure models

It is interesting to note how the traditional approach (E_P) and the indirect method lead to same results, and this is a confirmation of the validity of the assumptions made in Section 2.3 ($\Delta p_t Q \approx \dot{m} c_p \Delta T_t - \dot{m} T_{t,ref} \Delta s$). On the contrary, the direct method (which requires the integration of the entropy production in the computational domain) based on the turbulent kinetic energy production ($E_{S,g}$) leads to an overestimation of the available energy. This difference is not too significant for the $k-\omega$ model (about 2%), larger for the other turbulence models, and especially for the $k-\epsilon$ STD (about 9%). This result is in line with the differences encountered when estimating

the entropy generation in other applications: differences as large as 15% are not uncommon [70], and are due to the fact that CFD softwares do not solve the entropy equation, which therefore can be not strictly satisfied due to numerical errors, as explained in [71]. Lower discrepancies between the direct method and the other ones can be obtained when using the turbulent kinetic energy dissipation ($E_{S,d}$). The overestimation still remains high for $k-\varepsilon$ models, but it almost disappears for the $k-\omega$ SST model.

The larger estimation of the available energy from Spalart-Allmaras and $k-\varepsilon$ models is linked to the overestimation of local entropy generation (see Fig. 10), which is due to the different treatment of the boundary layer region, assumed fully turbulent [68]. On the contrary, the $k-\omega$ SST model adopts the standard $k-\varepsilon$ model only away from the walls and an improved formulation within the boundary layer [69], where viscous effects predominate over turbulent ones.

This difference in boundary layer treatment among $k-\omega$ SST and $k-\varepsilon$ STD model is highlighted in Fig. 12, that clearly shows higher intensity of non-dimensional entropy production in the boundary layer region for the $k-\varepsilon$ model. This overestimation is more evident near the suction side of the blade and near the trailing edge, at all spanwise positions from hub to tip.

The above results have been used to evaluate the turbine efficiencies defined in Section 2. The values reported in Fig. 13 are a direct consequence of the results in Figs. 8, 10, and 11. The aerodynamic efficiency η_{ad} is lower than the total-to-total efficiency η_{tt}, as the static pressure drop that appears in its denominator is larger than the total pressure drop that is used to calculate the first-law efficiency (the former includes the exit dynamic head, which in a Wells turbine is lost). The second-law efficiency (which theoretically should be approximately equal to the latter), has a very similar value only when the denominator is calculated using the indirect method, while it is lower when the direct method is selected. A further difference exists depending on whether the entropy generation $\dot{S}_G$ is calculated using the dissipation or the production of turbulent kinetic energy, being the latter slightly larger than the former (see Fig. 10). These differences are smaller for the $k-\omega$ model than for Spalart-Allmaras and $k-\varepsilon$ models. The second-law efficiency calculated using the turbulent kinetic energy dissipation with the $k-\omega$ SST model is remarkably close to the first-law efficiency.

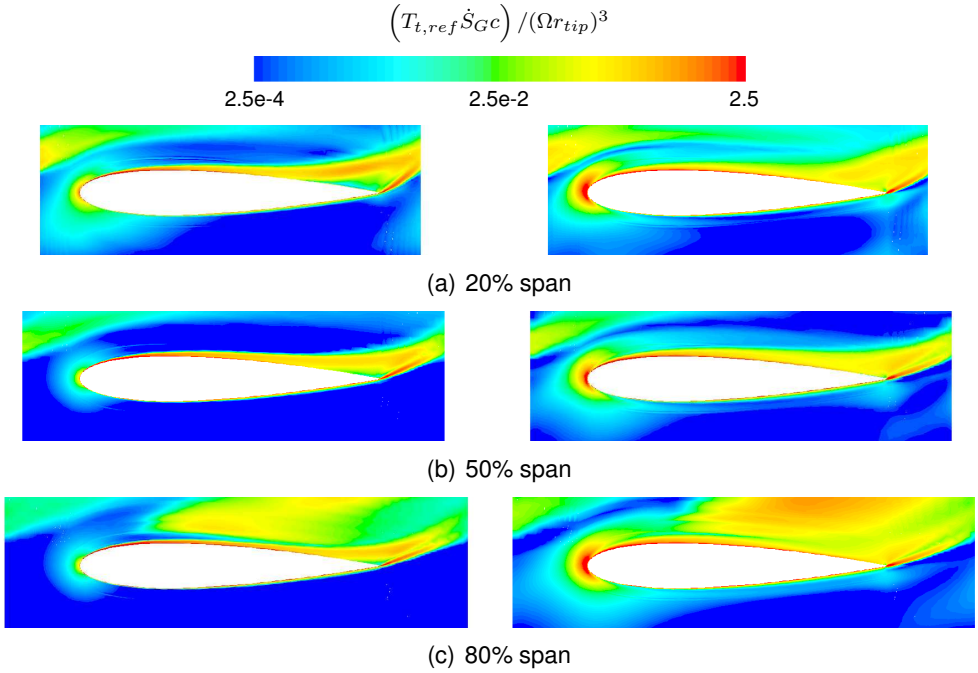

Fig. 12. Close-up view of the non-dimensional entropy production at several blade span positions for the maximum flow coefficient $\phi = 0.23$ calculated using $k-\omega$ SST (left) and $k-\varepsilon$ STD (right) models

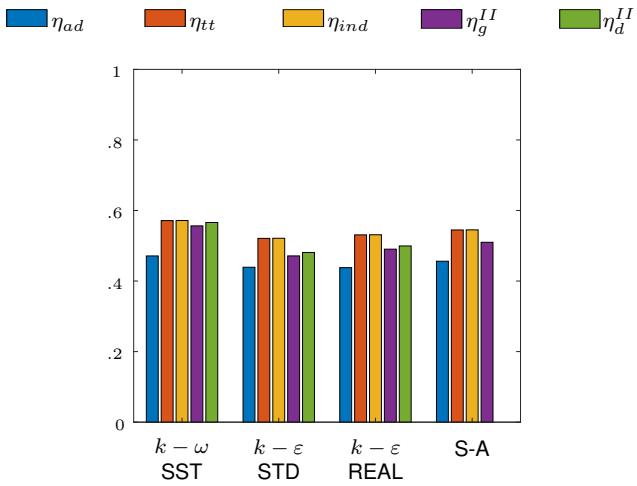

Fig. 13. Rotor efficiencies averaged on cycle and calculated with different turbulence closure models

5.2 Simulations with $\phi_{max} = 0.345$

Figure 14 reports the performance parameters of the Wells turbine with an operating (sinusoidal) cycle with a maximum flow coefficient sufficient to produce deep stall conditions.

When comparing the curves in Fig. 14, the $k-\varepsilon$ model in its standard formulation is unable to predict the turbine stall and the performance is always increasing with the flow coefficient (in

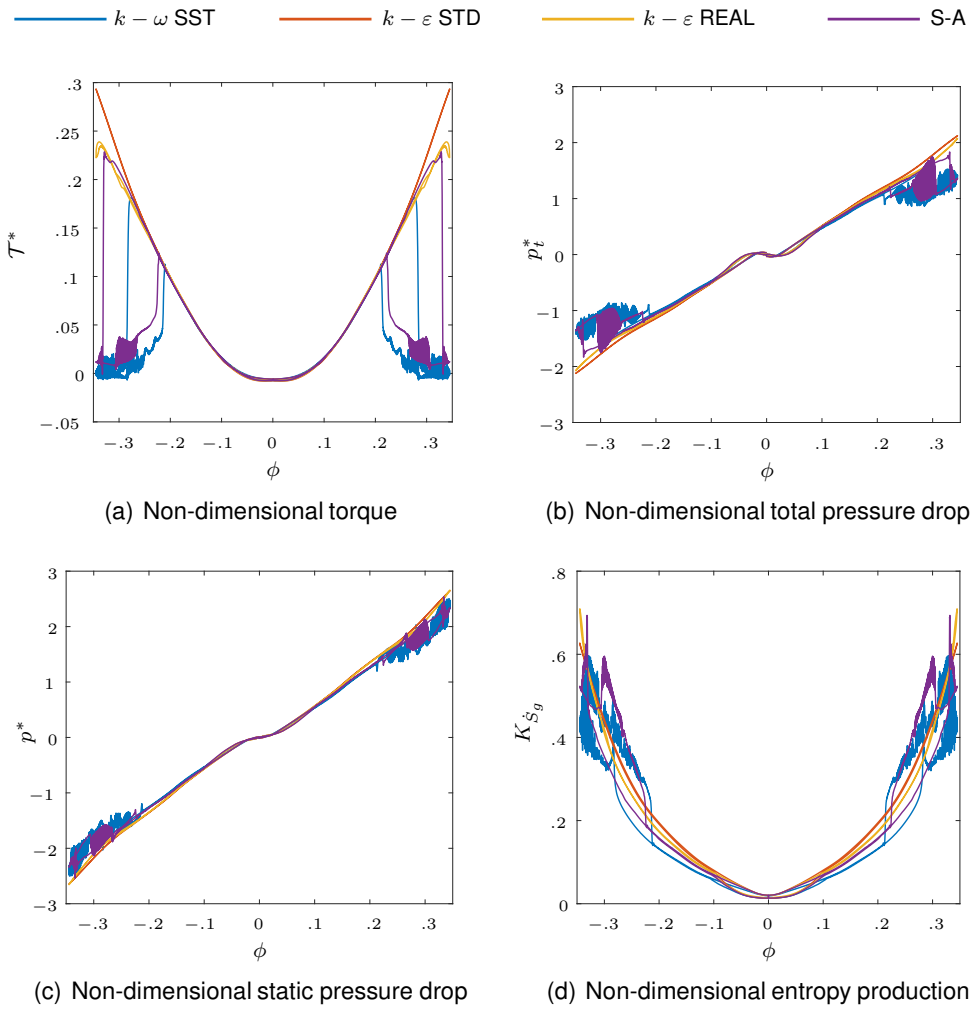

(a) Non-dimensional torque

(b) Non-dimensional total pressure drop

(c) Non-dimensional static pressure drop

(d) Non-dimensional entropy production

Fig. 14. Non-dimensional performance of the rotor with NACA0015 blade profile and $z = 6$ as a function of flow coefficient ϕ estimated with different turbulence closure models

the range considered here, i.e. $\phi = -0.345 \div 0.345$). The $k-\varepsilon$ REAL model predicts the presence of light stall for a ϕ just above 0.3. This is due to the difficulty of $k-\varepsilon$ models to correctly predict the separation of the boundary layer for low Reynolds number flows, in particular in the $k-\varepsilon$ STD formulation where the boundary layer is considered as fully turbulent [68]. $k-\omega$ SST and Spalart-Allmaras model predict the occurrence of stall (at ϕ equal to 0.28 and 0.32, respectively). After stall, the torque coefficient drops dramatically, and the entropy generation increases correspondingly. A high frequency oscillation in all performance parameters can be observed. During deceleration, the reattachment of the boundary layer, which corresponds to the exit from the stalled conditions, happens for a lower flow coefficient (equal to 0.2 and 0.22 for $k-\omega$ SST

and Spalart-Allmaras models). This leads to the presence of a hysteretic loop, which does not extend to the clean part of the curves, i.e. after reattachment. This hysteresis is not necessarily caused by dynamic effects, as a static stall hysteresis is well documented for many lifting surfaces [66, 67, 72, 73].

In order to better understand the difference between $k-\omega$ and $k-\varepsilon$ models predictions, Fig. 15 shows the vortical structures around the blade calculated with the two models. Iso-surfaces of Q-criterion, colored by the non-dimensional entropy production, are reported.

The comparisons in Fig. 15 show that the $k-\varepsilon$ model underestimates the large vortex located near the suction-side (SS) of the blade, as well as the large area of reversed flow near the trailing edge. The tip vortex grows for larger flow-coefficient values until it appears destroyed and a roll-up vortex can be observed on the same blade side near the trailing edge. The vortical structures located near the trailing edge when the blade is stalled are again smaller in $k-\varepsilon$ predictions than in $k-\omega$ ones. Both models show the entropy production growing with the flow-coefficient, as expected, with larger values being predicted by the $k-\varepsilon$ model especially near the blade surface, as previous observed in Fig. 12.

6 RESULTS - COMPARISONS AMONG DIFFERENT ROTOR GEOMETRIES

Five rotor geometries have been compared, with 3 rotor-tip solidities (0.48, 0.57, 0.67) and 3 blade thicknesses (NACA 0012, NACA 0015, NACA 0020 profiles). All the calculations have been performed using $k-\omega$ SST model under dynamic (sinusoidal) flow-conditions.

Starting from the global performance comparisons as in the previous section, Figs. 16 and 17 report the well-known non-dimensional parameters for the rotors with the same number of blades and with equal blade profile, respectively.

In Fig. 16, no significant modifications in performance can be noticed for a different blade profile thicknesses, while Fig. 17 highlights the strong effect of the rotor solidity on both torque- and pressure-coefficient. This is due to the blockage effect exerted by the rotor on the air-flow, directly dependent on the number of blades [47, 74, 75].

Fig. 18 compares the averaged non-dimensional entropy production for different rotor geome-

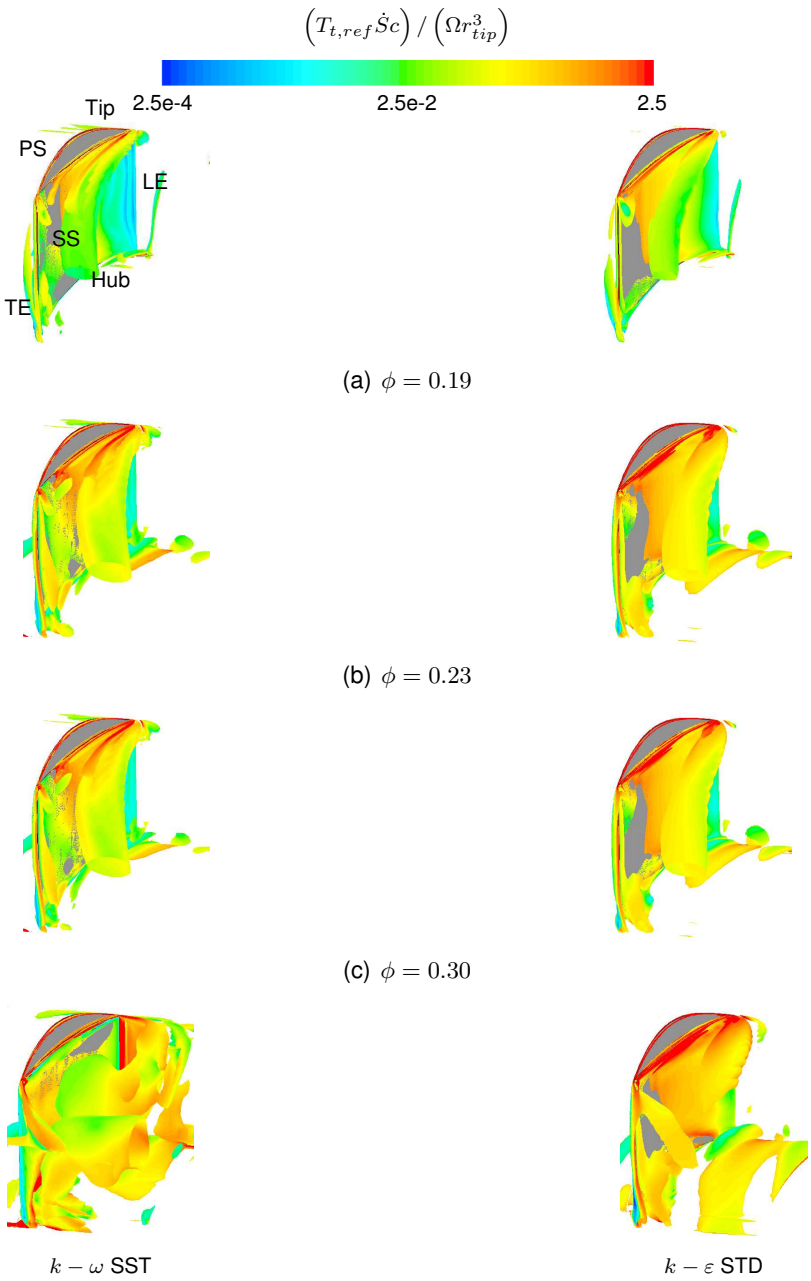

Fig. 15. Iso-surfaces of Q criterion (Q = 2.25e6 s^{-2}) coloured by non-dimensional entropy production

tries. The results are in agreement with the considerations drawn from the performance parameters comparisons, i.e. it is possible to state that the change in blade-profile thickness does not modify substantially the averaged rotor losses over a cycle and this is confirmed by a very similar entropy production for all 3 rotors with equal solidity. On the contrary, when the rotor solidity increases, the entropy production also increases and this fact is again related to the blockage effect

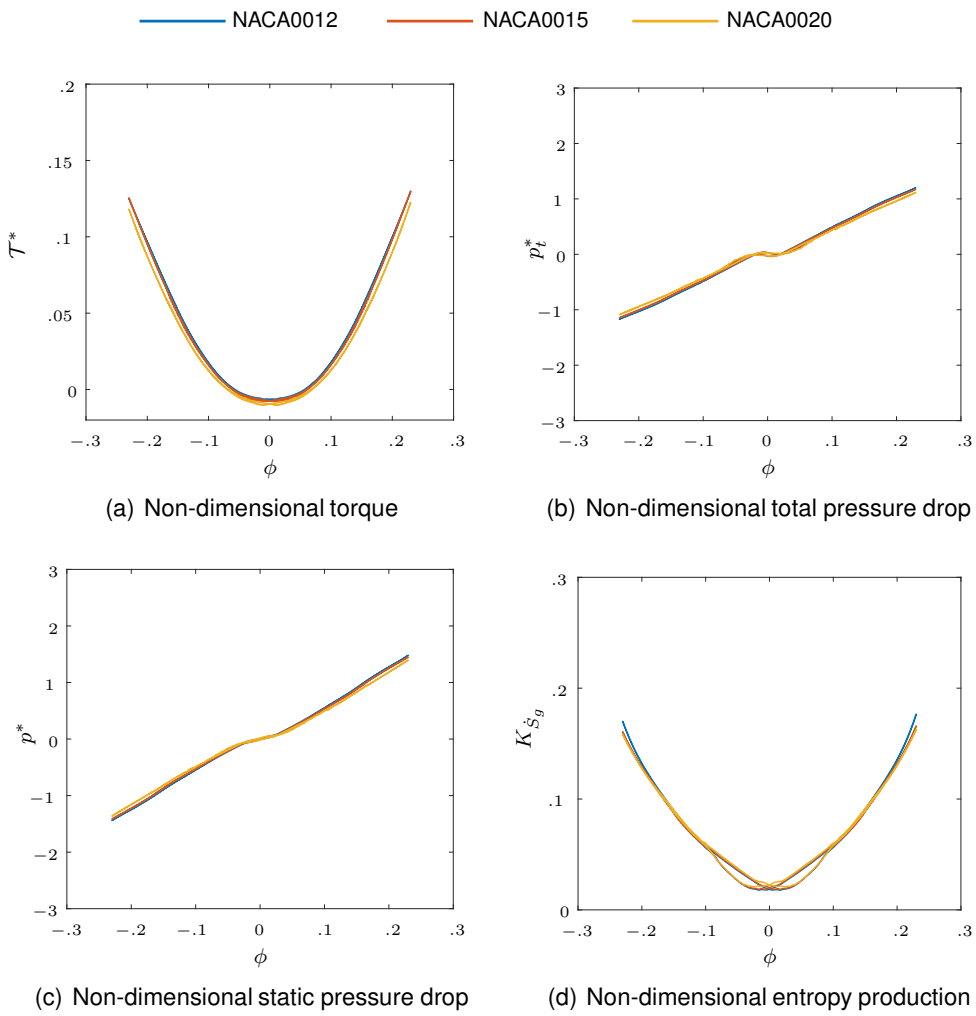

(a) Non-dimensional torque

(b) Non-dimensional total pressure drop

(c) Non-dimensional static pressure drop

(d) Non-dimensional entropy production

Fig. 16. Non-dimensional performance of the rotor with $z = 6$ and different blade profiles as a function of flow coefficient ϕ

exerted by the rotor on the flow.

The effect of the rotor solidity on the entropy production can be better observed in Fig. 19, where the local entropy production field around the blade is shown at different spanwise positions. The contour plots allow to make a qualitative analysis of the losses along the blade span. In particular, while low solidity rotors ($z = 5, 6$) shows similar amounts of entropy production at all spanwise positions, the highest solidity rotor ($z = 7$) experiences higher losses along the whole blade span. This is more evident in the hub region where the blades are the closest (i.e. the solidity assumes its highest value) and the blockage effect determines higher losses, as it can be determined by comparing the vortical structures in Fig. 20 for two different flow conditions. In

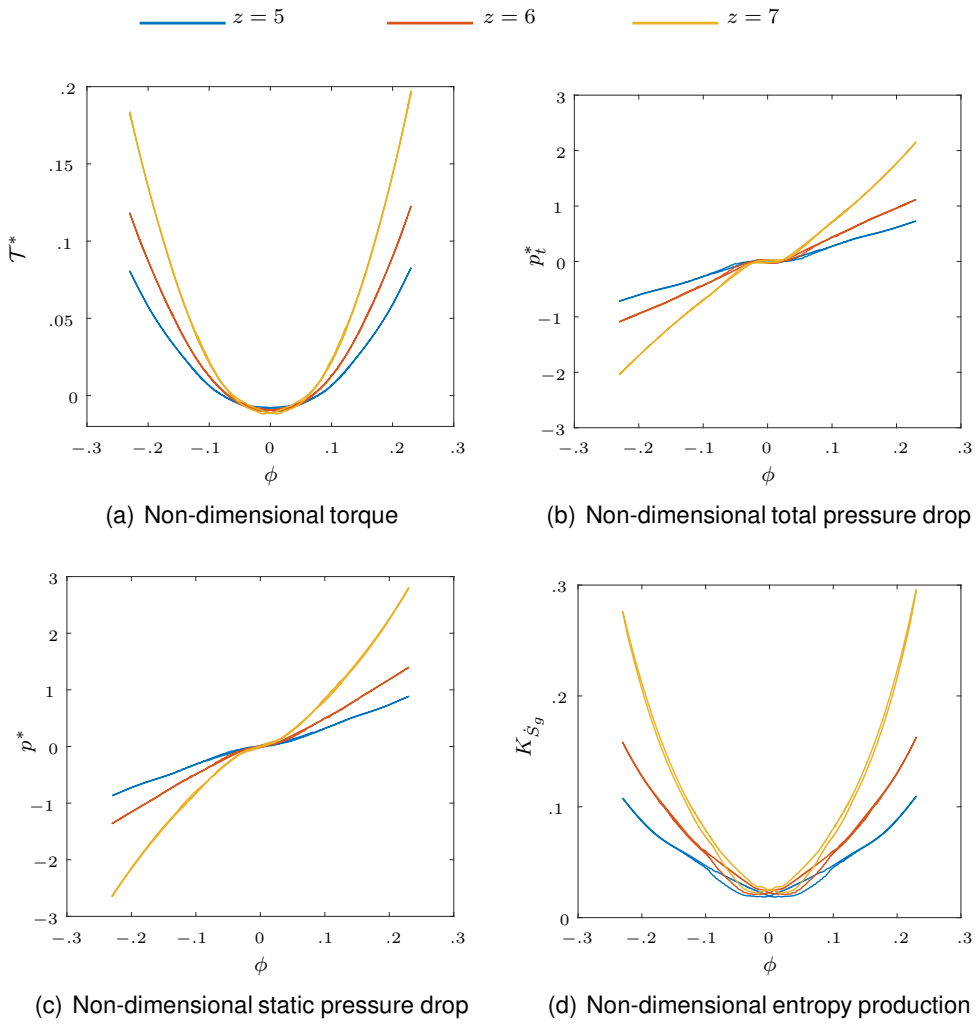

(a) Non-dimensional torque

(b) Non-dimensional total pressure drop

(c) Non-dimensional static pressure drop

(d) Non-dimensional entropy production

Fig. 17. Non-dimensional performance of the rotor with NACA0020 blade profile and different number of blades as a function of flow coefficient ϕ

fact, near the tip region, the entropy generation field around the 3 rotors looks more similar than for lower spanwise positions (Fig. 19), except for a more pronounced disruption of the vortical structures (Fig. 20) downstream the suction side.

Fig. 21 reports the energy production for the different geometries simulated, calculated as in Eqn. (39). The available energy calculated with the traditional and the indirect methods (E_P and E_E) lead to very close predictions. The differences are larger when the available energy is evaluated using the direct method, i.e. by integrating the production or destruction of turbulent kinetic energy inside the domain: it is interesting to note how this last estimation is always larger

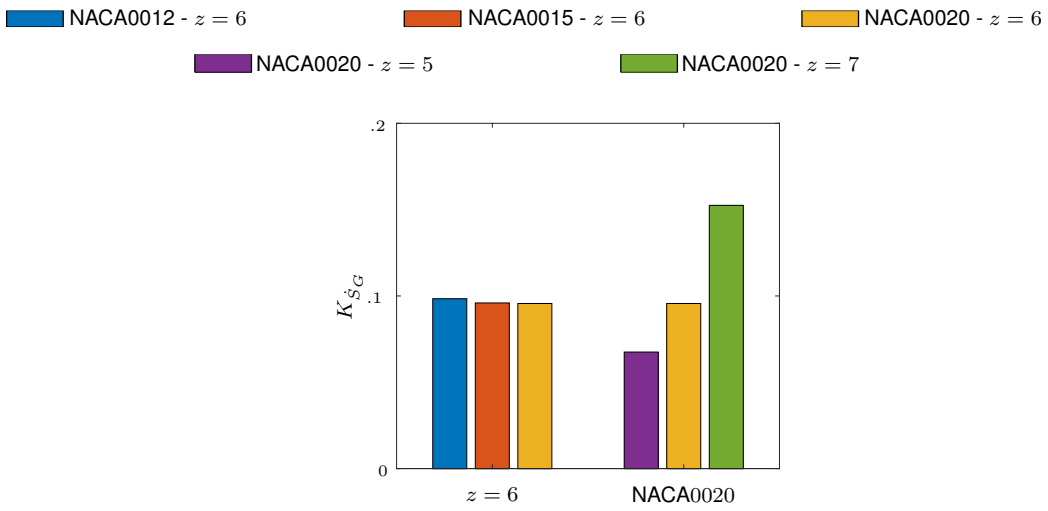

Fig. 18. Averaged non-dimensional entropy production rate evaluated near the rotor for different rotor geometries

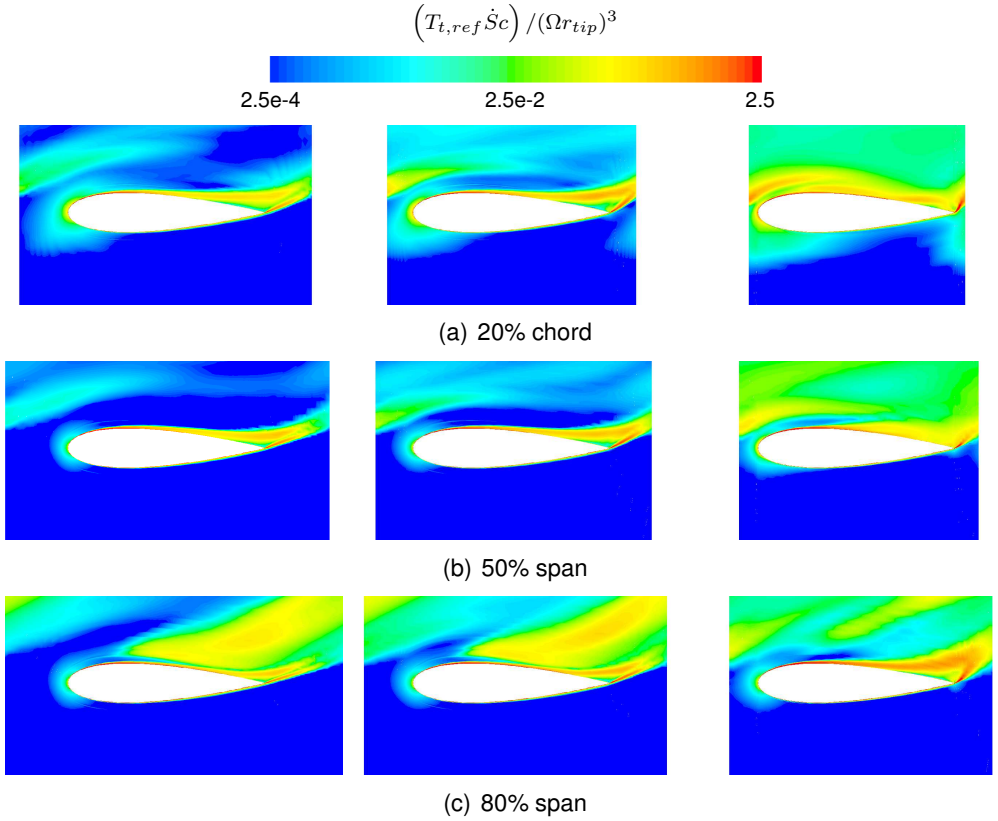

Fig. 19. Non-dimensional entropy production at several blade span positions for the maximum flow coefficient $\phi = 0.23$ and for rotor with $z = 5$ (left), $z = 6$ (centre) and $z = 7$ (right)

than the other two, except for the case of the rotor with the highest solidity. It is reasonable to assume larger numerical errors in the prediction of entropy generation for the rotor with the largest

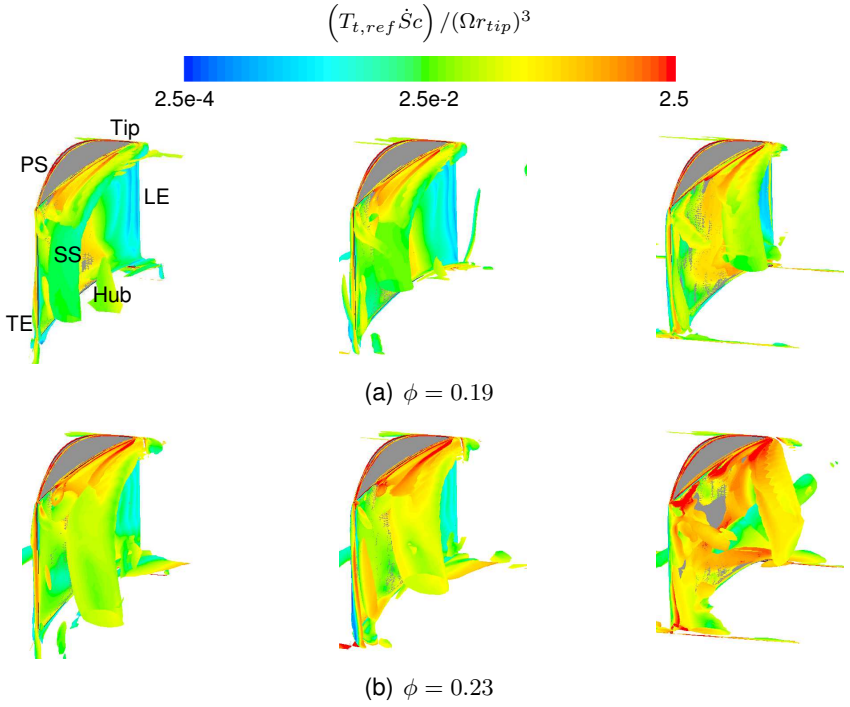

(a) $\phi = 0.19$

(b) $\phi = 0.23$

Fig. 20. Iso-surfaces of Q criterion ($Q = 2.25$e6 s^{-2}) coloured by non-dimensional entropy production for different flow conditions and for rotor with $z = 5$ (left), $z = 6$ (centre) and $z = 7$ (right)

solidity, where secondary flow structures are larger and more complex due to the smaller flow passage and higher pressure difference across the blade. The difference is in any case well below the values reported in other similar studies [36, 76].

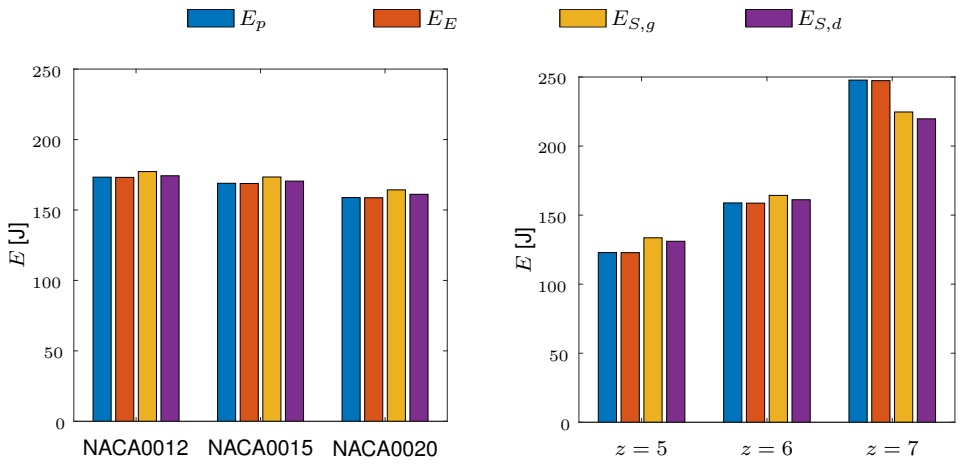

(a) Rotors with $z = 6$

(b) Rotors with NACA0020 blade profile

Fig. 21. Energy calculations averaged on a cycle for different rotor geometries

Finally, the mean rotor efficiencies reported in Fig. 22 allow to make a better comparison among the different geometries. The rotors with different blade thicknesses do not present significant variations in efficiency for the selected rotor solidity, i.e. 0.57: a small drop in efficiency is reported for the rotor with the largest thickness, as already reported in the experiments [43]. On the contrary, the solidity has a higher impact on the efficiency, and the 2 lower solidities represent the best solutions under these flow conditions. These results are comparable with the ones obtained in the experiments of [43] and [74].

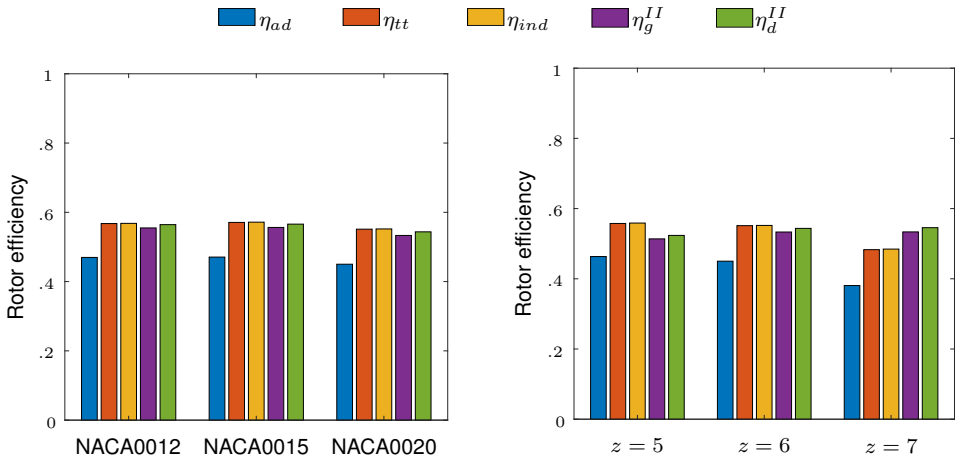

(a) Rotors with $z = 6$ (b) Rotors with NACA0020 blade profile

Fig. 22. Rotor efficiencies averaged on a cycle for all the tested geometries

7 CONCLUSIONS

This work attempts to clarify the underlying assumptions, as well as the methodologies available for estimation of the efficiency of the Wells turbine, with particular focus on the solution of RANS equations. In particular, it is shown that, under the assumptions typical for this type of turbomachinery, the so-called first- and second-law efficiencies give almost the same values. While the former requires the evaluation of the pressure drop across the machine, the latter can be calculated either by evaluating the entropy rise across the machine (the so-called *indirect* method [36]) or by integrating the local entropy generation rate in the domain (the *direct* method [36]). These two measures are theoretically equivalent, but some discrepancies can arise in CFD simulations

due to numerical errors, as entropy is not necessarily conserved in CFD solvers [71].

The results of the present work can be summarized as follows:

1. The first- and second-law efficiencies are equivalent measures for the efficiency of Wells turbines, at least when the assumption of incompressibility is valid
2. The available power $\Delta p_t Q$ is approximately equivalent to the net exergy $\dot{W} + T_{t,ref}\dot{S}_G$. This is theoretically valid for a machine evolving an incompressible flow, and has been verified in RANS simulations for a low speed Wells turbine, for several turbulence models and geometries
3. In numerical simulations, the net entropy flux is not strictly equal to the entropy generation rate inside the domain ($\theta_{ref}\dot{S}_{gen} \neq \dot{m}T_{t,ref}\Delta s$)
4. The error arising from the previous point is significantly smaller with the $k-\omega$ SST model than with $k-\epsilon$ (standard and realizable) models
5. The entropy generation rate can be estimated using either the production or dissipation of turbulent kinetic energy, and the difference between the 2 measures is small provided that the calculation is made in a large enough control volume
6. The (local) entropy generation rate provides a useful method for identifying the main sources of loss
7. The blade thickness has a minimal effect on the efficiency of the turbine under consideration. On the contrary, the efficiency is significantly affected by the solidity of the machine
8. Theoretical derivations and numerical analyses have been developed for a compressible flow in order to make the methodology applicable also to other problems. For the problems analyzed in this work, compressibility effects never accounted for more than 0.02% of the total entropy generation.

REFERENCES

[1] Pelc, R., and Fujita, R., 2002. "Renewable energy from the ocean". *Marine Policy,* **26**(6), pp. 471–479.

[2] Falcão, A., 2010. "Wave energy utilization: A review of the technologies". *Renewable and Sustainable Energy Reviews,* **14**(3), pp. 899–918.

[3] Wells, A., 1976. Fluid Driven Rotary Transducer - BR. Pat. 1595700.

[4] Curran, R., and Gato, L. M. C., 1997. "The energy conversion performance of several types of Wells turbine designs". *Proceedings of the Institution of Mechanical Engineers, Part A: Journal of Power and Energy,* **211**(2), pp. 133–145.

[5] Thakker, A., and Abdulhadi, R., 2008. "The performance of Wells turbine under bi-directional airflow". *Renewable Energy,* **33**(11), pp. 2467 – 2474.

[6] Paderi, M., and Puddu, P., 2013. "Experimental investigation in a Wells turbine under bi-directional flow". *Renewable Energy,* **57**, pp. 570–576.

[7] Dhanasekaran, T., and Govardhan, M., 2005. "Computational analysis of performance and flow investigation on Wells turbine for wave energy conversion". *Renewable Energy,* **30**(14), pp. 2129–2147.

[8] Setoguchi, T., Kinoue, Y., Kim, T., Kaneko, K., and Inoue, M., 2003. "Hysteretic characteristics of Wells turbine for wave power conversion". *Renewable Energy,* **28**(13), pp. 2113–2127.

[9] Torresi, M., Camporeale, S., and Pascazio, G., 2009. "Detailed CFD analysis of the steady flow in a Wells turbine under incipient and deep stall conditions". *Journal of Fluids Engineering, Transactions of the ASME,* **131**(7), pp. 0711031–07110317.

[10] Shehata, A., Saqr, K., Xiao, Q., Shehadeh, M., and Day, A., 2016. "Performance analysis of Wells turbine blades using the entropy generation minimization method". *Renewable Energy,* **86**, pp. 1123–1133.

[11] Shehata, A., Xiao, Q., El-Shaib, M., Sharara, A., and Alexander, D., 2017. "Comparative analysis of different wave turbine designs based on conditions relevant to northern coast of Egypt". *Energy,* **120**, pp. 450–467.

[12] Soltanmohamadi, R., and Lakzian, E., 2016. "Improved design of Wells turbine for wave energy conversion using entropy generation". *Meccanica,* **51**(8), pp. 1713–1722.

[13] Shaaban, S., 2012. "Insight analysis of biplane Wells turbine performance". *Energy Conversion and Management,* **59**, pp. 50 – 57.

[14] Gratton, T., Ghisu, T., Parks, G., Cambuli, F., and Puddu, P., 2018. "Optimization of blade profiles for the Wells turbine". *Ocean Engineering,* **169**, pp. 202–214.

[15] Kim, T., Setoguchi, T., Takao, M., Kaneko, K., and Santhakumar, S., 2002. "Study of turbine with self-pitch-controlled blades for wave energy conversion". *International Journal of Thermal Sciences,* **41**(1), pp. 101–107.

[16] Starzmann, R., and Carolus, T., 2013. "Effect of blade skew strategies on the operating range and aeroacoustic performance of the Wells turbine". *Journal of Turbomachinery,* **136**(1), 09.

[17] Licheri, F., Climan, A., Puddu, P., Cambuli, F., and Ghisu, T., 2018. "Numerical study of a Wells turbine with variable pitch rotor blades". Vol. 148, pp. 511–518.

[18] Mohamed, M., Janiga, G., Pap, E., and Thvenin, D., 2011. "Multi-objective optimization of the airfoil shape of Wells turbine used for wave energy conversion". *Energy,* **36**(1), pp. 438 – 446.

[19] Mohamed, M., and Shaaban, S., 2013. "Optimization of blade pitch angle of an axial turbine used for wave energy conversion". *Energy,* **56**, pp. 229 – 239.

[20] Halder, P., Rhee, S. H., and Samad, A., 2017. "Numerical optimization of Wells turbine for wave energy extraction". *International Journal of Naval Architecture and Ocean Engineering,* **9**(1), pp. 11 – 24.

[21] Nazeryan, M., and Lakzian, E., 2018. "Detailed entropy generation analysis of a Wells turbine using the variation of the blade thickness". *Energy,* **143**, pp. 385 – 405.

[22] Shehata, A., Xiao, Q., Selim, M., Elbatran, A., and Alexander, D., 2017. "Enhancement of performance of wave turbine during stall using passive flow control: First and second law analysis". *Renewable Energy,* **113**, pp. 369–392.

[23] Suzuki, M., Arakawa, C., and Tagori, T., 1984. "Fundamental studies on Wells turbine for wave power generator (1st report, the effect of solidity, and self-starting)". *Bulletin of JSME,* **27**(231), pp. 1925–1931.

[24] Gato, L., and de O. Falcão, A., 1988. "Aerodynamics of the Wells turbine". *International Journal of Mechanical Sciences,* **30**(6), pp. 383 – 395.

[25] Folley, M., Curran, R., and Whittaker, T., 2006. "Comparison of limpet contra-rotating Wells turbine with theoretical and model test predictions". *Ocean Engineering,* **33**(8), pp. 1056 – 1069.

[26] Raghunathan, S., Tan, C. P., and Ombaka, O. O., 1985. "Performance of the Wells self-

rectifying air turbine". *Aeronautical Journal,* **89**, dec, pp. 369–379.

[27] Dixon, S. L., and Hall, C. A., 2010. *Fluid Mechanics and Thermodynamics of Turbomachinery*, 6 ed. Elsevier, Inc.

[28] Raghunathan, S., Tan, C., and Wells, N., 1982. "Theory and performance of a Wells turbine". *Journal of Energy,* **6**(2), pp. 157–160.

[29] Gato, L. M. C., and Curran, R., 1996. "Performance of the biplane Wells turbine". *Journal of Offshore Mechanics and Arctic Engineering,* **118**(3), 08, pp. 210–215.

[30] Gato, L. M. C., and Falcão, A. F. d. O., 1984. "On the theory of the Wells turbine". *Journal of Engineering for Gas Turbines and Power,* **106**(3), 07, pp. 628–633.

[31] Bejan, A., 2006. *Advanced engineering thermodynamics*, 3 ed. John Wiley & Sons, Inc.

[32] Ghisu, T., Cambuli, F., Puddu, P., Mandas, N., Seshadri, P., and Parks, G. T., 2018. "Numerical evaluation of entropy generation in isolated airfoils and Wells turbines". *Meccanica,* **53**(14), Nov., p. 3437.

[33] Ferziger, J. H., and Perič, M., 2002. *Computational methods for fluid dynamics*. Springer-Verlag.

[34] Versteeg, H. K., and Malalasekera, W., 2007. *An introduction to computational fluid dynamics: the finite volume method*. Pearson Education Limited.

[35] Anderson, D. A., Tannehill, J. C., and Pletcher, R. H., 1984. *Computational fluid mechanics and heat transfer*. Taylor & Francis Inc.

[36] Herwig, H., and Kock, F., 2007. "Direct and indirect methods of calculating entropy generation rates in turbulent convective heat transfer problems". *Heat and Mass Transfer,* **43**(3), Jan, pp. 207–215.

[37] Moore, J., and Moore, J. G., 1983. "Entropy production rates from viscous flow calculations: part i - a turbulent boundary layer flow.". *American Society of Mechanical Engineers (Paper)*(83-GT-70).

[38] Iandoli, C. L., Sciubba, E., and Zeoli, N., 2008. "The computation of the entropy generation rate for turbomachinery design applications: some theoretical remarks and practical examples". *International Journal of Energy Technology and Policy,* **6**(1), pp. 64–95.

[39] Jin, Y., and Herwig, H., 2015. "Turbulent flow in rough wall channels: Validation of rans models". *Computers & Fluids,* **122**, pp. 34 – 46.

[40] Asinari, P., Fasano, M., and Chiavazzo, E., 2016. "A kinetic perspective on k$-\varepsilon$ turbulence model and corresponding entropy production". *Entropy,* **18**(4).

[41] Shih, T.-H., Liou, W. W., Shabbir, A., Yang, Z., and Zhu, J., 1995. "A new k-ε eddy viscosity model for high Reynolds number turbulent flows". *Computers & Fluids,* **24**(3), pp. 227 – 238.

[42] ANSYS, INC., 2013. *ANSYS Fluent User's Guide*, 15.0 ed. Southpointe, 275 Technology Drive, Canonsburg, PA 15317, Nov.

[43] Setoguchi, T., Takao, M., and Kaneko, K., 1998. "Hysteresis on Wells turbine characteristics in reciprocating flow". *International Journal of Rotating Machinery,* **4**(1), pp. 17–24.

[44] , 2018. Performance Testing of an Axial Flow Fan Designed for Air-Cooled Heat Exchanger Applications, Vol. Volume 1: Aircraft Engine; Fans and Blowers; Marine of *Turbo Expo: Power for Land, Sea, and Air*. V001T09A005.

[45] Sun, T., Petrie-Repar, P., Vogt, D. M., and Hou, A., 2019. "Detached-Eddy Simulation Applied to Aeroelastic Stability Analysis in a Last-Stage Steam Turbine Blade". *Journal of Turbomachinery,* **141**(9), 05.

[46] Hill, D. J., and Defoe, J. J., 2020. "Scaling of Incidence Variations With Inlet Distortion for a Transonic Axial Compressor". *Journal of Turbomachinery,* **142**(2), 01.

[47] Watterson, J., and Raghunathan, S., 1998. "Computed effects of solidity on Wells turbine performance". *JSME International Journal, Series B: Fluids and Thermal Engineering,* **41**(1), pp. 177–183.

[48] Hashem, I., Abdel Hameed, H., and Mohamed, M., 2018. "An axial turbine in an innovative oscillating water column (owc) device for sea-wave energy conversion". *Ocean Engineering,* **164**, pp. 536 – 562.

[49] Das, T. K., and Samad, A., 2018. "The Effect of Midplane Guide Vanes in a Biplane Wells Turbine". *Journal of Fluids Engineering,* **141**(5), 11.

[50] Kumar, P. M., and Samad, A., 2019. "Introducing gurney flap to wells turbine blade and performance analysis with openfoam". *Ocean Engineering,* **187**, p. 106212.

[51] Valizadeh, R., Abbaspour, M., and Rahni, M. T., 2020. "A low cost hydrokinetic wells turbine system for oceanic surface waves energy harvesting". *Renewable Energy,* **156**, pp. 610 – 623.

[52] Ghisu, T., Puddu, P., and Cambuli, F., 2016. "Physical explanation of the hysteresis in Wells turbines: A critical reconsideration". *Journal of Fluids Engineering, Transactions of the ASME,* **138**(11).

[53] Ghisu, T., Puddu, P., and Cambuli, F., 2017. "A detailed analysis of the unsteady flow within a wells turbine". *Proceedings of the Institution of Mechanical Engineers, Part A: Journal of Power and Energy,* **231**(3), pp. 197–214.

[54] Ghisu, T., Puddu, P., Cambuli, F., and Virdis, I., 2017. "On the hysteretic behaviour of Wells turbines". *Energy Procedia,* **126**, pp. 706–713.

[55] Ghisu, T., Cambuli, F., Puddu, P., Virdis, I., Carta, M., and Licheri, F., 2020. "A critical examination of the hysteresis in wells turbines using computational fluid dynamics and lumped parameter models". *Journal of Offshore Mechanics and Arctic Engineering,* **142**(5).

[56] Ghisu, T., Cambuli, F., Puddu, P., Virdis, I., and Carta, M., 2019. "Discussion on "Unsteady RANS simulations of Wells turbine under transient flow conditions" by Hu and Li". *ASME Journal of Offshore Mechanics and Arctic Engineering,* **141**(4), pp. 045501–045501–5.

[57] Brito-Melo, A., Neuman, F., and Sarmento, A. J. N. A., 2008. "Full-scale data assessment in OWC Pico plant". In Proceedings of the International Journal of Offshore and Polar Engineering, Vol. 18, pp. 27–34.

[58] Garrido, A. J., Otaola, E., Garrido, I., Lekube, J., Maseda, F. J., Liria, P., and Mad er, J., 2015. "Mathematical Modeling of Oscillating Water Columns Wave-Structure Interaction in Ocean Energy Plants". *Mathematical Problems in Engineering*, pp. –.

[59] Freitas, C., 1993. "Journal of Fluids Engineering editorial policy statement on the control of numerical accuracy". *Journal of Fluids Engineering, Transactions of the ASME,* **115**(3), pp. 339–340.

[60] Ghisu, T., Puddu, P., Cambuli, F., Mandas, N., Seshadri, P., and Parks, G., 2018. "Discussion on Performance analysis of Wells turbine blades using the entropy generation minimization

method by Shehata, A. S., Saqr, K. M., Xiao, Q., Shahadeh, M. F. and Day, A.". *Renewable Energy,* **118**, pp. 386–392.

[61] Carr, L. W., McAlister, K. W., and McCroskey, W. J., 1977. Analysis of the development of dynamic stall based on oscillating airfoil experiments. Tech. Rep. NASA Technical Note D-8382, NASA AMES Research Center.

[62] Ericsson, L. E., and Reding, J. P., 1988. "Fluid mechanics of dynamic stall: Part 1 unsteady flow concepts". *Journal of Fluids and Structures,* **2**, pp. 1–33.

[63] Barakos, G. N., and Drikakis, D., 2003. "Computational study of unsteady turbulent flows around oscillating and ramping aerofoils". *International Journal for Numerical Methods in Fluids,* **186**, pp. 163–186.

[64] Cambuli, F., Ghisu, T., Virdis, I., and Puddu, P., 2019. "Dynamic interaction between owc system and wells turbine: A comparison between cfd and lumped parameter model approaches". *Ocean Engineering,* **191**, p. 106459.

[65] Ghisu, T., Cambuli, F., Puddu, P., Virdis, I., Carta, M., and Licheri, F., 2020. "A lumped parameter model to explain the cause of the hysteresis in owc-wells turbine systems for wave energy conversion". *Applied Ocean Research,* **94**, p. 101994.

[66] Mittal, S., and Saxena, P., 2000. "Prediction of hysteresis associated with the static stall of an airfoil". *AIAA journal,* **38**(5), pp. 933–935.

[67] Sarlak, H., Fr re, A., Mikkelsen, R., and Srensen, J., 2018. "Experimental investigation of static stall hysteresis and 3-dimensional flow structures for an nrel s826 wing section of finite span". *Energies,* **11**(6).

[68] Menter, F., 1992. "Performance of popular turbulence models for attached and separated adverse pressure gradient flows". *AIAA Journal,* **30**(8), pp. 2066–2072.

[69] Menter, F., 1994. "Two-equation eddy-viscosity turbulence models for engineering applications". *AIAA Journal,* **32**(8), pp. 1598–1605.

[70] Li, D., Wang, H., Qin, Y., Han, L., Wei, X., and Qin, D., 2017. "Entropy production analysis of hysteresis characteristic of a pump-turbine model". *Energy Conversion and Management,* **149**, pp. 175 – 191.

[71] Fidkowski, K. J., Ceze, M. A., and Roe, P. L., 2012. "Entropy-based drag-error estimation and mesh adaptation in two dimensions". *Journal of Aircraft,* **49**(5), pp. 1485–1496.

[72] Mizoguchi, M., Kajikawa, Y., and Itoh, H., 2014. "Static stall hysteresis of low-aspect-ratio wings". *32nd AIAA Applied Aerodynamics Conference*.

[73] Modarres, R., Peters, D., and Gaskill, J., 2016. "Dynamic stall model with circulation pulse and static hysteresis for NACA 0012 and VR-12 airfoils". *Journal of the American Helicopter Society,* **61**(3).

[74] Thakker, A., and Abdulhadi, R., 2007. "Effect of blade profile on the performance of Wells turbine under unidirectional sinusoidal and real sea flow conditions". *International Journal of Rotating Machinery,* **2007**.

[75] Torresi, M., Camporeale, S., Strippoli, P., and Pascazio, G., 2008. "Accurate numerical simulation of a high solidity Wells turbine". *Renewable Energy,* **33**(4), pp. 735 – 747.

[76] Jin, Y., and Herwig, H., 2015. "Turbulent flow in rough wall channels: validation of RANS models". *Computers and Fluids,* **122**, pp. 34–46.